LIGHT-WATER-REACTOR SAFETY
RESEARCH PROGRAM:
QUARTERLY PROGRESS REPORT

October—December 1978

ARGONNE NATIONAL LABORATORY, ARGONNE, ILLINOIS

ARGONNE NATIONAL LABORATORY
9700 South Cass Avenue
Argonne, Illinois 60439

LIGHT-WATER-REACTOR SAFETY
RESEARCH PROGRAM:
QUARTERLY PROGRESS REPORT
October–December 1978

Robert G. Sachs, Laboratory Director
Jack A. Kyger, Associate Laboratory Director

Date Published: April 1979

TABLE OF CONTENTS

479 004

TABLE OF CONTENTS

ABSTRACT

This progress report summarizes the Argonne National Laboratory work performed during October, November, and December 1978 on water-reactor-safety problems The following research and development areas are covered: (1) Loss-of-coolant Accident Research: Heat Transfer and Fluid Dynamics; (2) Transient Fuel Response and Fission-product Release Program; and (3) Mechanical Properties of Zircaloy Containing Oxygen.

I. LOSS-OF-COOLANT ACCIDENT RESEARCH: HEAT TRANSFER AND FLUID DYNAMICS

Responsible Section Managers:
H. F. Fauske, R. E. Henry, and P. A. Lottes, RAS

A. Transient Critical Heat Flux (J. C. M. Leung and R. E. Henry, RAS)

1. Steady-state CHF in Inlet-peaking Profile

A total of 72 CHF measurements were obtained using Freon-11 in Test Section IV which has an inlet peaking heat flux profile as shown in Fig. I.1 with a peak-to-average of 1.35. CHF was slowly approached by slowly increasing the test-section power while maintaining constant inlet pressure and flow rate. Considerable inlet throttling was found necessary to eliminate the low-frequency oscillation, and no CHF data reported were induced by flow oscillation. CHF indications were detected by wall thermocouples and were identified by either rapid temperature excursion (mostly under high power and high velocity) or oscillation (low power and low velocity) of the wall. In all cases, CHF was observed to originate near the exit of the heated tube and not in the highest heat-flux zone. The data fell within the following experiment ranges:

Pressure, P	1.5-2.9 MPa
Mass velocity, G	707-2750 kg/m²·s
Critical power, q_c	7-15 kW
Inlet subcooling, Δh_{in}	7.7-40 J/g
Dryout quality, x_{DO}	0.16-0.5
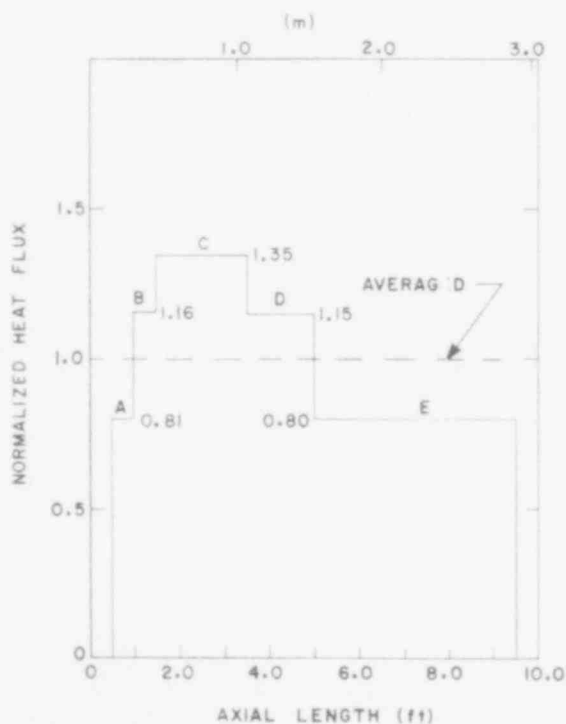
Fig. I.1

Test Section IV with Inlet-skewed Heat-flux Profile. ANL Neg. No. 900-78-1029.

In a previous study,[1] the CISE Freon correlation[2] (hereon designed as CISE-CNEN correlation) was found to predict CHF very well in a uniformly heated round tube, yielding a mean error of 0.5% and an rms error of only 3.6%. This correlation has the form

$$\varphi_{CHF} = A - Bx_{in} \tag{1}$$

where

$$A = fn(G, P, D, L),$$
$$B = fn(G, P, D, L),$$

and

$$x_{in} = inlet\ quality.$$

Note that the critical heat flux increases linearly with inlet subcooling. However, Eq. 1 can also be written in terms of the exit quality x_{out} with the use of the energy equation,

$$x_{out} = \frac{4\varphi L}{GDh_{fg}} + x_{in}. \tag{2}$$

Hence Eq. 1 becomes, after substitution,

$$\varphi_{CHF} = C - Dx_{out}. \tag{3}$$

where

$$C = fn(G, P, D, L)$$

and

$$D = fn(G, P, D, L).$$

Here the critical heat flux decreases with exit quality. These two forms of correlation described above will, of course, give the same answer when used for predicting CHF for uniform heat flux. However, if they are applied to nonuniform heat-flux conditions, different values of φ_{CHF} will be obtained. A number of hypotheses have been proposed to predict CHF in the nonuniform axial heat-flux case. Four such hypotheses that have been tested using the present data are outlined briefly below.

a.   The Total (Overall)-power Hypothesis[3]

This hypothesis suggests that the total power that can be fed to the tube with nonuniform heating will be the same as for a uniformly heated

tube of the same diameter D and length L, and with the same inlet conditions. Hence the critical power q_c is given by

$$q_c = \pi D L \varphi_{CHF},$$ (4)

where φ_{CHF} is the critical heat flux predicted using Eq. 1. Here no prediction of the location of the critical conditions is made with this method.

b. The Local-conditions Hypothesis[3]

This hypothesis suggests that CHF occurs in the channel where the unique local heat flux/local quality relationship (i.e., Eq. 3) is first satisfied. It can be employed in the following two ways:

(1) Use the measured power in the heat balance to calculate the local quality, which is subsequently used to calculate CHF using Eq. 3. The heat balance is written as

$$x(z) = \frac{4 \int_0^z \varphi(z) dz}{GD} + x_{in}.$$ (5)

This method is most convenient to be adapted in a thermal-hydraulic computer code, which is used to predict local flow parameters in transient situations.

(2) Assume that the test section power is not known, and therefore we must solve Eqs. 3 and 5 simultaneously. One way is to gradually increase the power until, at some point within the channel, the conditions for the two equations are satisfied, thereby giving the CHF (or power) and the critical location.

c. The Boiling-length Hypothesis

Lee and Obertelli[4] reported that CHF is independent of tube length for a given exit quality in uniformly heated tubes. This implies that the tube may be divided into two lengths; over the first subcooled length (λ), the liquid is raised to saturation [$x(\lambda) = 0$], and over the second length (L_B), the quality is raised from zero to the dryout quality. The only function of λ is to heat the incoming fluid up to the saturation condition at the appropriate heat flux.[3] In fact, the CISE correlation[2] was originally proposed in the functional form

$$x_{out} = \frac{a L_B}{b + L_B}.$$ (6)

This suggests that the dryout quality is a function of boiling length L_B, where the upstream history is contained implicitly. Lahey and Gonzalez-Santalo[5] show that the Tong-F factor method[6] in the limiting case of maximum upstream memory (or influence) reduces to the equation

$$\varphi_u = \frac{1}{L_{B_c}} \int_\lambda^{\lambda + L_{B_c}} \varphi(z)dz. \tag{7}$$

This implies that, φ_u, the equivalent uniform CHF, is given by the nonuniform heat-flux profile averaged over the critical boiling length, L_{B_c}. One further interesting observation is pointed out in Ref. 5, in that, if Eqs. 3, 5, and 7 are combined, a term similar to Eq. 6 is arrived at. In other words, the boiling-length hypothesis and the empirical methods proposed by Tong[6] and Silvestri[7] are equivalent in the limit. Two methods were used to compare with data:

(1) Compare the experimental average heat flux φ_u over the critical boiling length with the heat flux φ_{CHF} predicted by the CISE-CNEN correlation.

(2) For any CHF location ($z_{CHF} = \lambda + L_{B_c}$), predict the critical power from the formula

$$q_c = \left(\pi D \varphi_{CHF} L_{B_c} + \frac{\pi D^2}{4} G \Delta h_{in}\right)/F, \tag{8}$$

where

$$F = \frac{1}{L} \int_0^{z_{CHF}} P(z)dz. \tag{9}$$

Here F is the ratio of integral power upstream of the CHF location to the total power, and $P(z)$ is the peak-to-average power factor. However, L_{B_c} is unknown and an initial guess has to be made. Once q_c is calculated from Eq. 8, an updated value for L_{B_c} is solved for by the equation

$$\int_0^{z_{CHF} - L_{B_c}} \left(\frac{q_c}{\pi D L}\right) P(z)dz = \frac{GD \Delta h_{in}}{4}. \tag{10}$$

By successive substitution, the solution is found to converge rather quickly and the method yields both critical power and CHF location using an iterative process.

d. The Equivalent-length Hypothesis

Lee[8] suggested that an equivalent length L_{eq} can be defined at a CHF point such that

$$L_{eq}\varphi(z_{CHF}) = \int_0^{z_{CHF}} \varphi(z)dz, \tag{11}$$

where $\varphi(z_{CHF})$ is the local CHF on the nonuniformly heated tube at a distance z_{CHF} from the inlet. To predict critical power, the CHF correlation is used to estimate φ_{CHF} using the inlet conditions, tube diameter, and the equivalent length.

$$q_c = (\pi D\varphi_{CHF}L_{eq})/F. \tag{12}$$

In the actual calculation of L_{eq}, Eq. 11 is not used, since φ is unknown. Instead we use

$$L_{eq} = \int_0^{z_{CHF}} \frac{P(z)}{P(z_{CHF})} dz. \tag{13}$$

With this method, a direct solution is obtained for critical power and critical location.

Figure I.2 summarizes the three integral hypotheses graphically. The results of the comparison, as shown in Figs. I.3-I.6 give a direct test of the various hypotheses:

The total-power hypothesis (a) shows little scatter of data, but underpredicts by about 7% in Fig. 3.

The first approach for the local-conditions hypothesis in Fig. I.4 [b(1)] yields large scatter and poor prediction.

The first approach for the boiling-length hypothesis in Fig. I.5 [c(1)] slightly overpredict the data by about 7%.

The equivalent-length hypothesis (d) shown in Fig. I.6 is able to predict th data to within -1.0% in overall error and therefore appears to be the most satisfactory method.

The reason the local condition method appears to predict so poorly is that, from Eq. 3, φ_{CHF} is seen to be a strong function of x_{out}; i.e., a slight variation in x_{out} results in a large change in φ_{CHF}. For the present system, a 10% increase in x_{out} causes a reduction of more than 30% in φ_{CHF}. However, this is the approach widely taken to predict CHF conditions during a transient. The accurate prediction of local flow parameters by the thermal-hydraulic code plays an important role in the subsequent CHF evaluation using

the local-conditions hypothesis, and as shown by the comparison here, large error still prevails. However, if the simultaneous solution of the CHF correlation and the heat balance is sought [i.e., in the method outlined in b(2)], much better agreement results, as shown in Fig. I.7. Here totally different conclusions are arrived at, depending on how we use the local-conditions hypothesis.
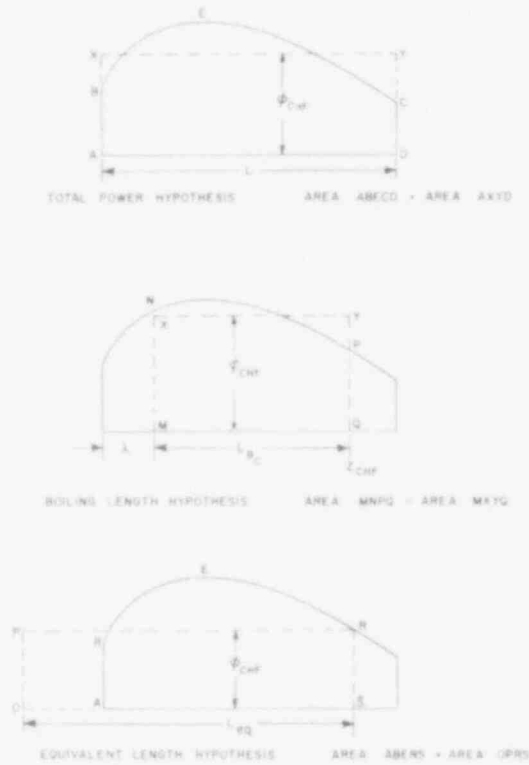
Fig. I.2

Graphical Representation of Various CHF Hypotheses. ANL Neg. No. 900-79-39.
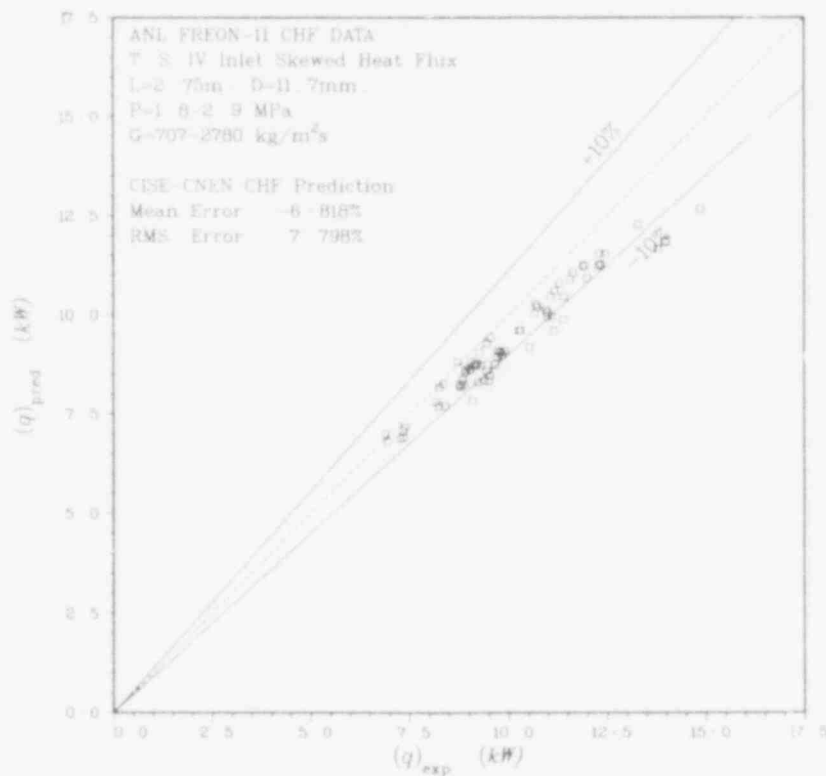
Fig. I.3. Test of Total-power Hypothesis. ANL Neg. No. 900-79-284.
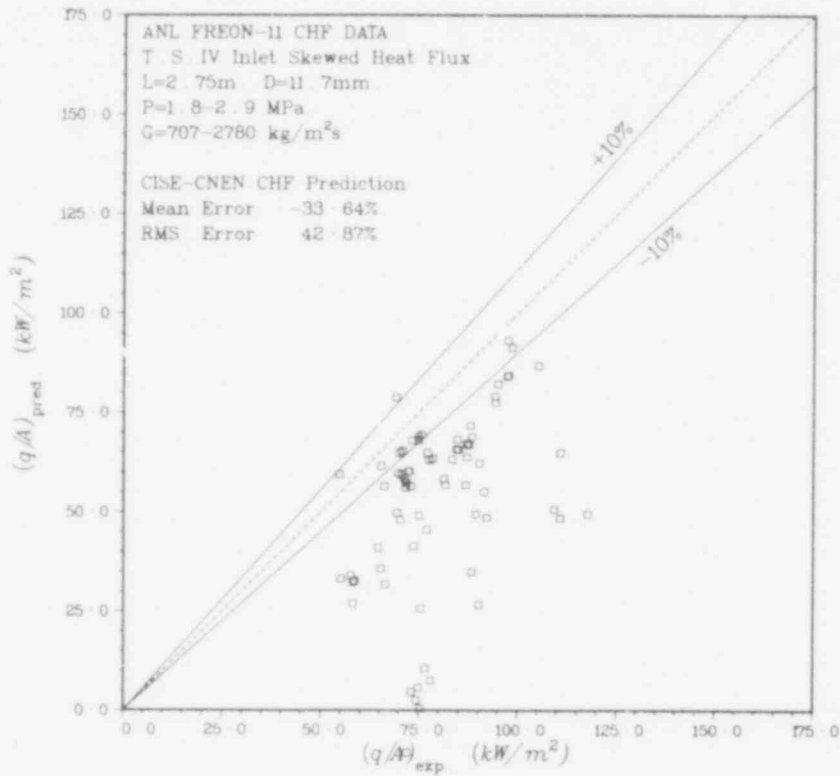
Fig. 1.4. Test of Local-conditions Hypothesis. ANL Neg. No. 900-79-288.
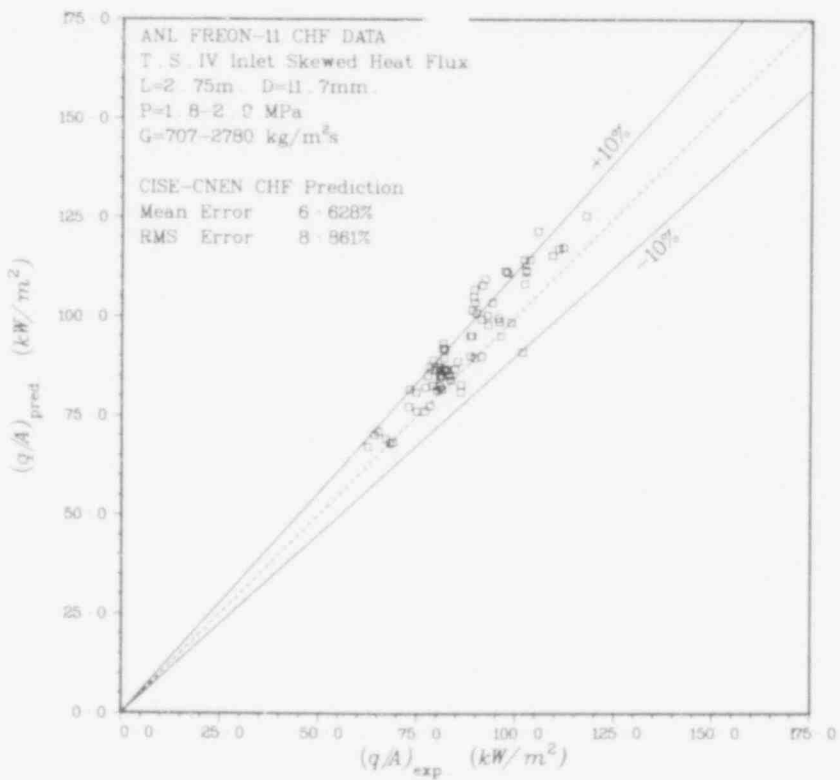
Fig. 1.5. Test of Boiling-length Hypothesis. ANL Neg. No. 900-79-282.

8
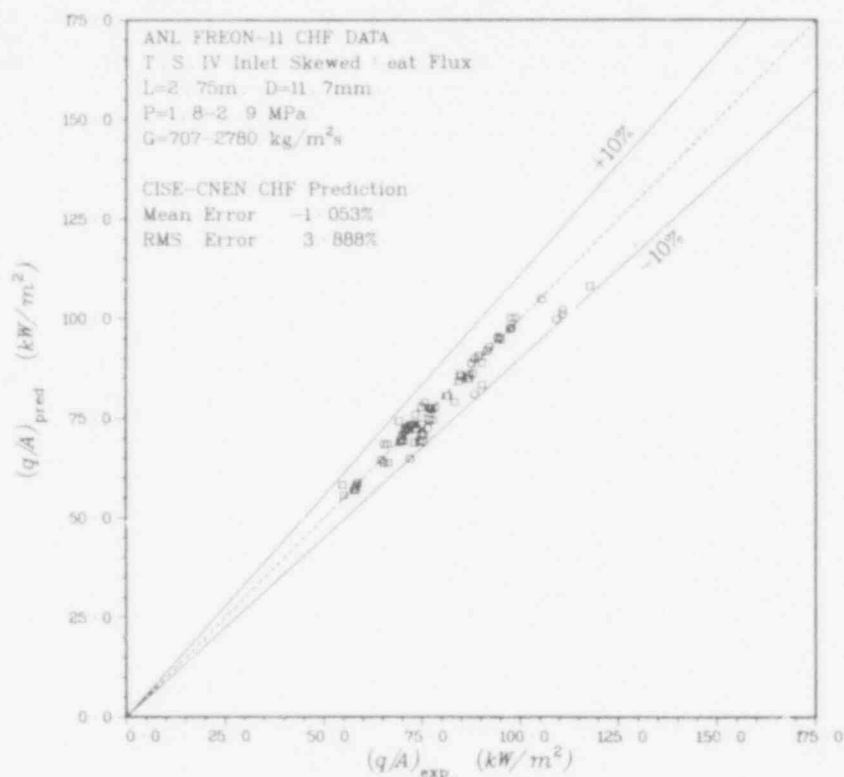
Fig. I.6. Test of Equivalent-length Hypothesis. ANL Neg. No. 900-79-283.
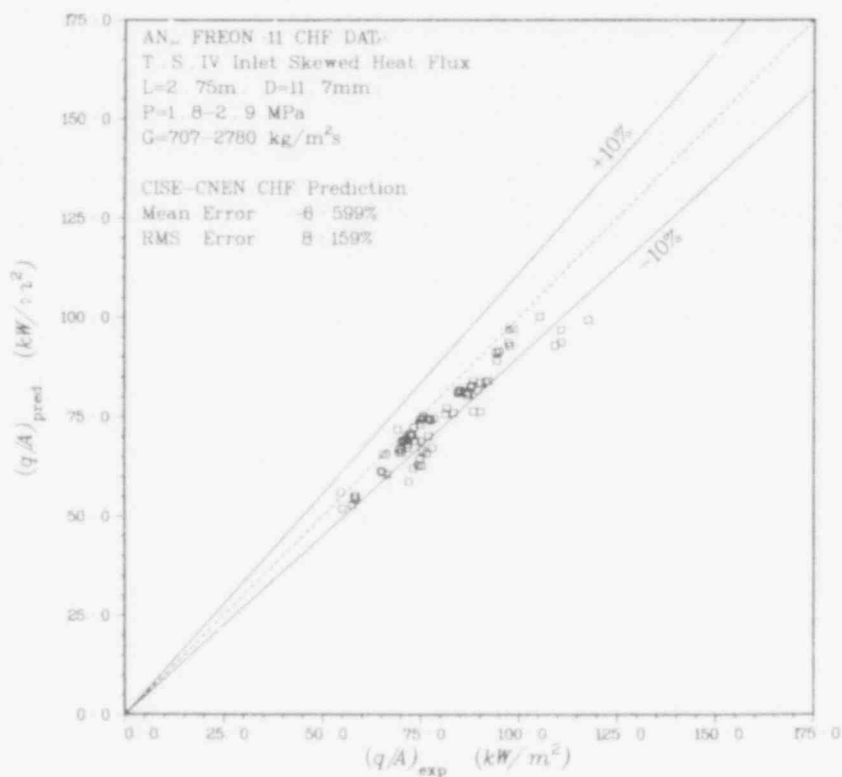
Fig. I.7. Prediction of CHF Using Local-conditions
Hypothesis. ANL Neg. No. 900-79-283.

Finally, the critical power as predicted by the second approach for the boiling-length hypothesis [c(2)] and the equivalent-length hypothesis (d) is shown in Figs. I.8 and I.9, respectively. The error analysis remains essentially unchanged from earlier plots (Figs. I.5 and I.6). Although the equivalent-length hypothesis is shown to yield the best result, the conclusion is best made after analyzing the symmetric stepped heat-flux data[9] and the exit skewed heat-flux data.

2. Transient Critical Heat Flux

Transient CHF tests have been conducted with the skewed inlet power profile shown in Fig. I.1. The results of the high- and low-pressure tests are shown in Figs. I.10 and I.11. The low-pressure test (2.21 MPa) demonstrated rapid CHF in the region from the inlet up to 0.5 m; the times to CHF are shown in Fig. I.10. The high-pressure tests (2.76 MPa), Fig. I.11, exhibited early CHF in the bottom 1.4 m, which includes the two highest heat-flux zones C and D.
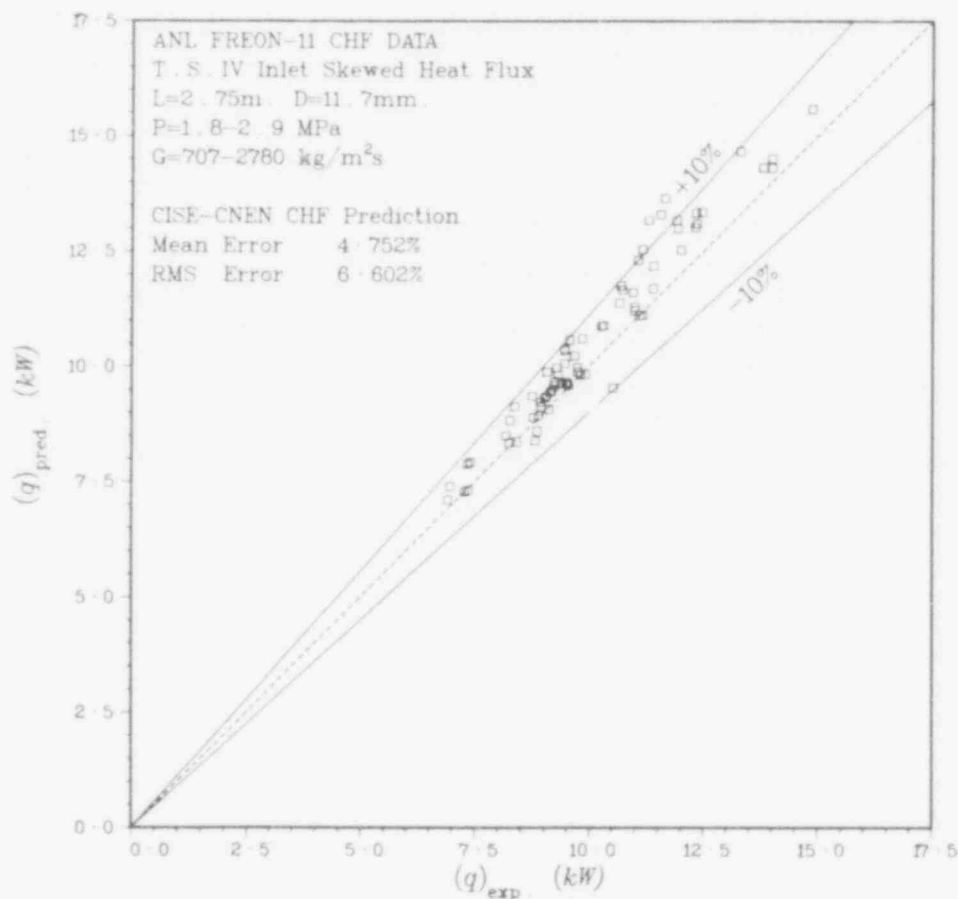
Fig. I.8. Prediction of Critical Power Using Boiling-length Hypothesis. ᴸ Neg. No. 900-79-287.
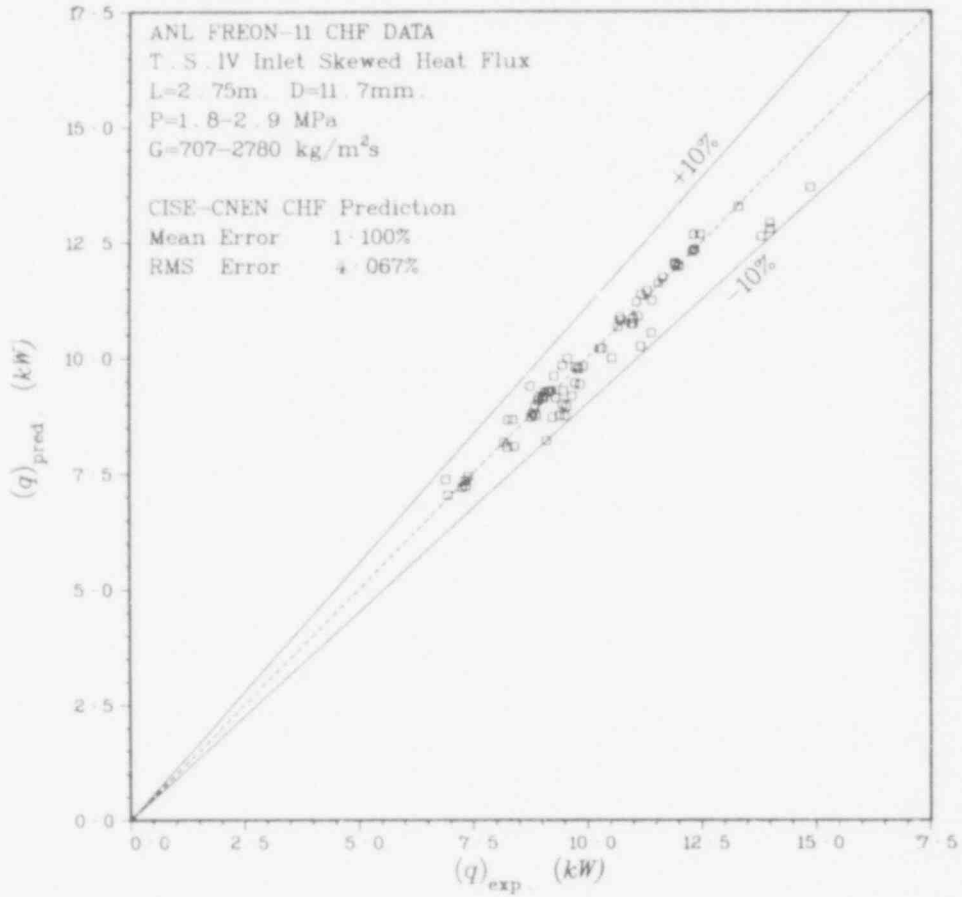
Fig. I.9. Prediction of Critical Power Using Equivalent-length
Hypothesis. ANL Neg. No. 900-79-286.
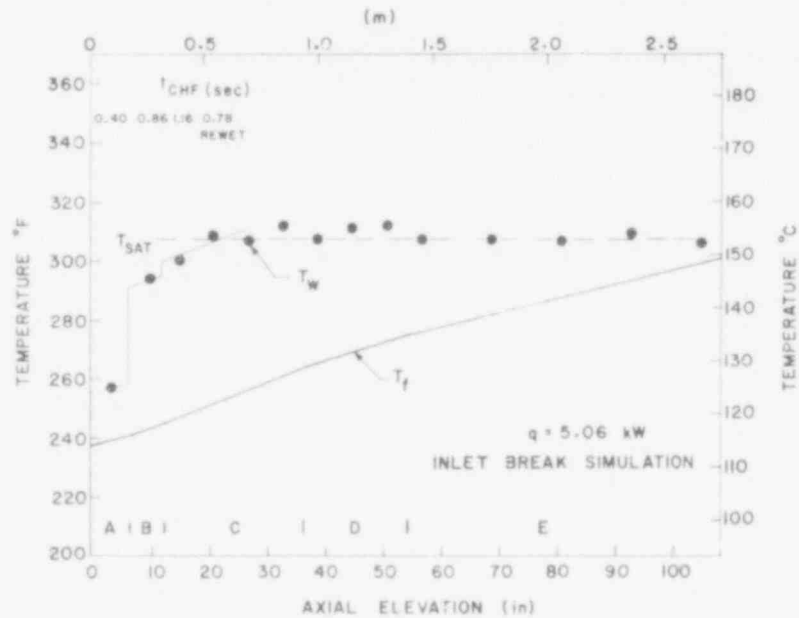
Fig. I.10. Measured Wall Temperatures and Blowdown CHF Behavior
at 2.21 MPa (320 psia). ANL Neg. No. 900-78-1176.
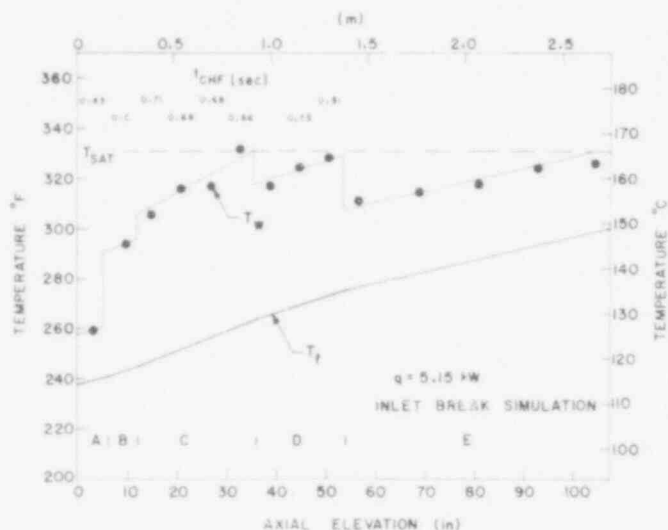
Fig. I.11

Measured Wall Temperatures and Blowdown CHF Behavior at 2.76 MPa (400 psia). ANL Neg. No. 900-78-1178.

As an additional test of the site-deactivation model, another test was conducted at high pressure (2.72 MPa), but in this test, the deactivation was not accomplished at the hot standby condition, i.e., inlet temperature of 113°C and system pressure of 2.72 MPa. Instead, the initial system pressure was 2.21 MPa, and the test section was brought up to full power and full flow at these conditions. This resulted in a wall-temperature profile similar to that shown in Fig. I.10. Under these conditions, the sites were activated for the test-section locations above 0.5 m.

Following this activation, the pressure was then increased up to 2.72 MPa in about 15 s, and the system was operated at steady state for about 20 s before blowdown transient was initiated. As can be seen from the times to CHF shown in Fig. I.12, this test experiences early CHF from the test-section inlet up to about 0.7 m, which is a length considerably less than that experienced by the other high-pressure test. Since the only difference between these two high-pressure experiments was the deactivation of the surface cavities, this set of tests clearly illustrates the importance of such deactivation on the extended cooling of the fuel-rod surfaces during the LOCA of an inlet-pipe rupture.

Fig. I.12

Measured Wall Temperatures and Blowdown CHF Behavior with Reactivated Sites. ANL Neg. No. 900-78-1177.
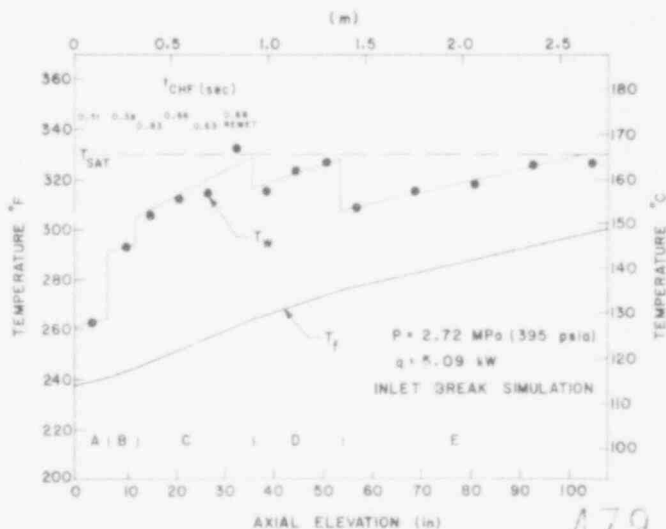
B. Reflood Tests (Y. S. Cha, R. E. Henry, and P. A. Lottes, RAS)

Several tests were performed with relatively low average inlet velocity (~2.6 cm/s) and with initial test-section temperature maintained at 702°C (1295°F). These tests are supplements to those reported previously which had approximately the same inlet average velocity but lower initial test-section temperature (548°C). The operating conditions for these tests are shown in Table I.1, where $T_{18,i}$ is the initial temperature measured by thermocouple 18, f is the frequency of forced oscillation, $\overline{V}_i$ is the average inlet velocity to the test section, and β_f is the opening position of the micrometer valve between the test section and the water-supply tank for forward flow. For all the tests, the inlet water temperature was 65°C (150°F), the water-supply tank pressure for forward flow was maintained at 0.205 MPa (15 psig), the pressure in the water-receiving tank for reverse flow was 0.1 MPa (1 atm), the opening position for the micrometer valve between the test section and the receiving tank was four turns, and the temperatures at the discharge end of the test section were heated up to about 121°C (250°F) before each test.

TABLE I.1. Operating Conditions for Runs 48-51

Run No.	$T_{18,i}$ (°C)	f (Hz)	$\overline{V}_i$ (cm/s)	Power (kW)	β_f (No. of turns)
48	704	0.292	2.54	0	2.25
49	702	0.939	2.64	0	2.00
50	702	3.030	2.55	0	2.50
51	702	0	2.64	0	1.70

Figure I.13 shows the variation of quench time with axial distance for these tests. In general, the differences in quench-front velocity were small and appeared only during the second half of these tests. The quench-front velocity increased with the frequency of forced oscillation. This observation is consistent with those reported previously with the same inlet average velocity. The test without forced oscillation (Run 51) appeared to have the fastest quench-front velocity. This was due to the slightly higher inlet average velocity for Run 51 as compared to Run 50.

Table I.2 shows the measured values of the change in liquid level in the water-supply tank ($\Delta \ell_f$), the change in liquid level in the water-receiving tank ($\Delta \ell_r$), the time required to complete the test (Δt), and the change in liquid level in the recirculation tank ($\Delta \ell_c$). The total amount of liquid collected in the recirculation tank ($\Delta \ell_c$) for these tests was slightly larger than for those tests with the same inlet average velocity but with initial test-section temperature equal to

Fig. I.13

Quench Time vs Axial Distance for Runs 48-51. ANL Neg. No. 900-79-60.

548°C. However, the values of $\Delta \ell_e$ for these tests were much smaller than those tests with approximately the same initial test-section temperature but with relatively high inlet average velocities (6.4 and 20 cm/s).

TABLE I.2. Experimentally Determined Values of $\Delta \ell_f$, $\Delta \ell_r$, Δt, and $\Delta \ell_e$ for Runs 48-51

Run No.	$\Delta \ell_f$ (cm)	$\Delta \ell_r$ (cm)	Δt (s)	$\Delta \ell_e$ (cm)
48	25.40	6.03	482.0	6.37
49	26.83	7.30	468.6	6.98
50	31.75	11.59	501.4	7.10
51	17.94	0	430.0	5.90

Up to now, all the forced-oscillation tests were performed by using the solenoid valve and the wave generator as the flow-control mechanism. This system is capable of closing or opening the flow passages in relatively short time. This fast action created irregular shapes in the flow profiles as measured by the orifice plates, and it was difficult to determine the average instantaneous flow over a cycle of oscillation. The present setup was modified by using a ball-valve system so that cleaner flow profiles can be obtained. A schematic of the new system is shown in Fig. I.14.

Fig. I.14. Schematic of Reflood Test Facility with Ball-valve System. ANL Neg. No. 900-78-909 Rev. 1.

14

 The arrangement shown in Fig. I.14 differs from pi̇̇ ̇ ̇us arrangements in two respects: (1) Two ball valves, driven by a variable-speed motor instead of a solenoidal valve and a wave generator, control the flow to and from the test section; (2) an orifice plate is placed between the test section and the ball-valve system, so that both the forward and the reverse flow are measured by this orifice plate. This is different from the previous arrangement, which used two orifice plates to measure the forward and the reverse flow, respectively.

 Typical flow profiles under cold conditions (i.e., without heating up the test section) are shown in Figs. I.15-I.17 at three different frequencies of oscillation. The dashed lines in these figures corresponding to zero-flow condition, which has an output of 2.5 V from the differential pressure transducer. These flow profiles are cleaner than those obtained by using the solenoid valve.
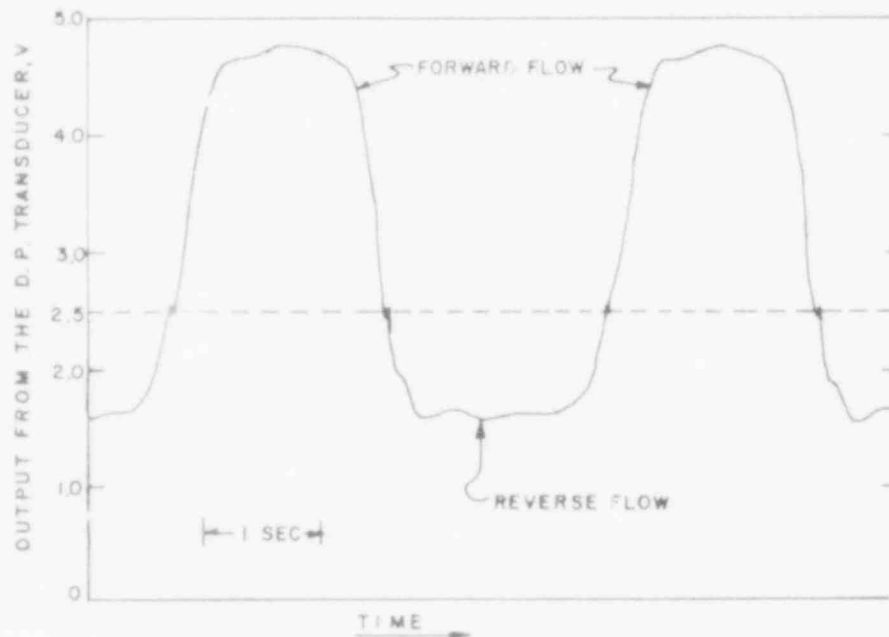
Fig. I.15

Output from Differential Pressure Transducer vs Time for Test with $f = 0.274$ Hz

Fig. I.16

Output from Differential Pressure Transducer vs Time for Test with $f = 1.034$ Hz
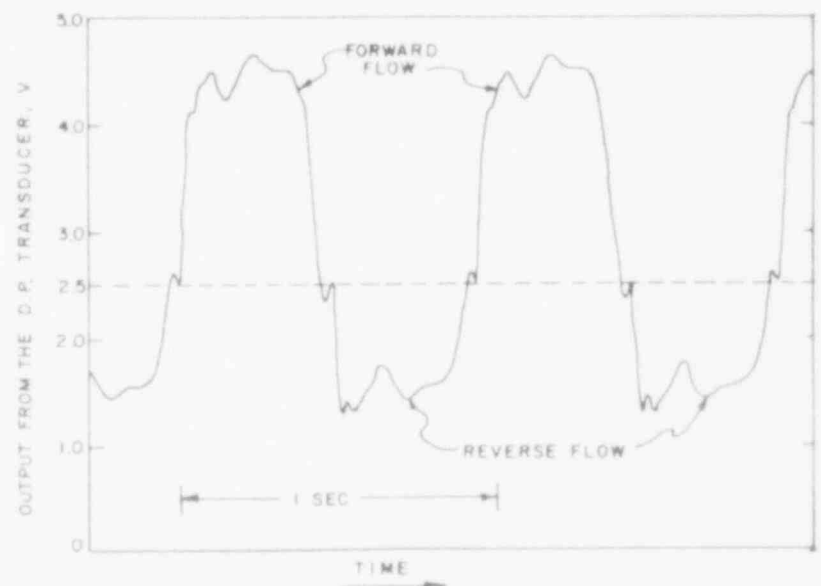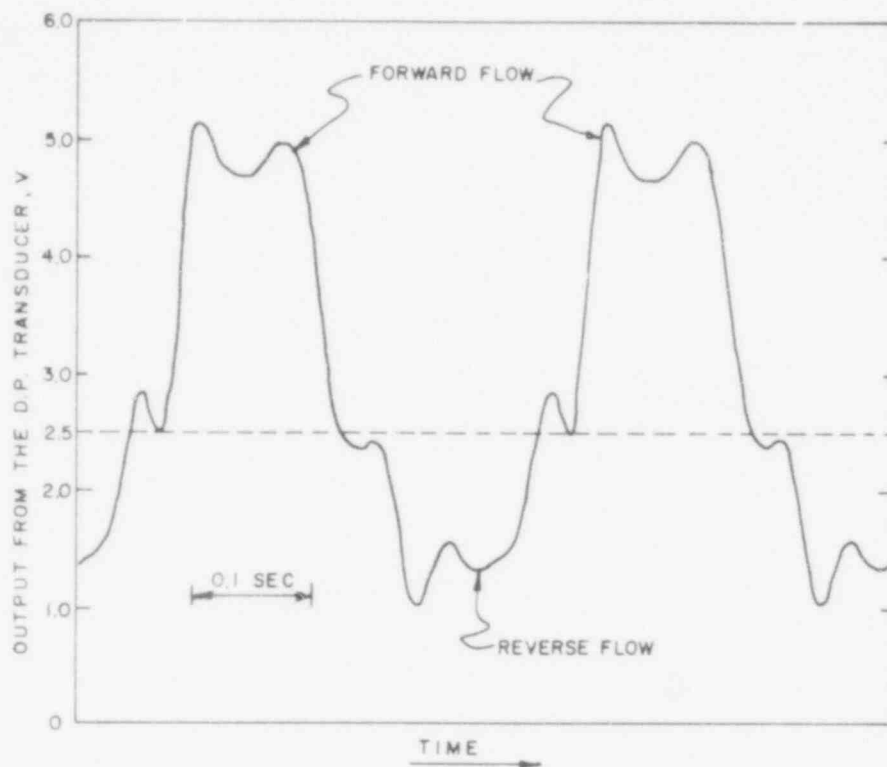
The orifice plate was calibrated under steady-state conditions in both
the forward and the reverse flow directions. It is important to verify that the
steady-state calibration data can be applied to the oscillatory (transient) con-
ditions in the range of interest of the present reflood tests. To demonstrate
this, we performed cold tests by closing the throttle valve in the reverse flow
line so that there was only flow in the forward direction during the entire test.
Water leaving the test section was collected in the recirculation tank. The
increase in the amount of water in the recirculation tank, divided by the total
number of cycles of oscillation during the test, gives the amount of flow to the
test section per cycle. This number can be used to check the results obtained
by graphically integrating the flow profile using the steady-state calibration
data.

The results are shown in
Table I.3, where V_m is the mea-
sured increase in the amount of
water in the recirculation tank per
cycle, V_c is the calculated volume
flow into the test section per cycle
obtained by integrating the flow
profile, and $\Delta\tau$ is the time interval
used in performing the integra-

TABLE I.3. Comparison between V_m and V_c at
Three Frequencies of Oscillation

f (Hz)	V_m (cm³/cycle)	V_c (cm³/cycle)	% Difference	$(\Delta\tau \cdot f)^{-1}$
2.857	1.149	1.201	4.54	28
0.990	3.423	3.317	3.22	20
0.294	11.152	11.238	0.77	34

tion. The last column in Table I.3 indicates the total number of intervals
used in performing the integration during one cycle of oscillation.

As shown in Table I.3, the maximum error introduced by using the
steady-state calibration data is less than 5%. This error can be reduced by

increasing the number of intervals used in the integration of the flow profile. The results shown in Table I.1 also indicate that there is a slight increase in percentage error as the frequency of oscillation is increased. However, in the range of interest of the present reflood tests (f = 0.3 to 3.0 Hz), the errors introduced by using the steady-state calibration data are not considered significant.

Several tests were performed by using the ball-valve system with relatively low inlet average velocity (~2.5 cm/s). The operating conditions for these tests are shown in Tables I.4 and I.5, where β_r is the opening position of the throttle valve located between the test section and the receiving tank, P_s is the pressure of the supply tank. P_r is the pressure of the receiving tank, $\overline{V}_f$ is the mean velocity for the forward flow averaged over the half-cycle of oscillation, and $\overline{V}_r$ is the mean velocity for the reverse flow averaged over the half-cycle of oscillation. The relation among these average velocities is

$$\overline{V}_i = (\overline{V}_f - \overline{V}_r)/2.$$

TABLE I.4. Operating Conditions for Runs 52-58
Using the Ball-valve System

Run No.	$T_{is,i}$ (°C)	f (Hz)	Power (kW)	β_f (turns)	β_r (turns)	P_s (MPa)	P_r (MPa)
52	704	0.237	0	1.85	2.0	0.411	0.101
53	699	1.111	0	1.80	2.0	0.411	0.101
54	702	2.780	0	1.75	2.0	0.411	0.101
55	704	0	0	1.15	0	0.411	0.101
56	707	0.298	0	2.3	3.0	0.411	0.067
57	713	0.983	0	2.2	3.0	0.411	0.067
58	707	2.780	0	2.2	3.0	0.411	0.067

TABLE I.5. Measured Quantities for Runs 52-58
Using the Ball-valve System

Run No.	$\Delta \ell_f$ (cm)	$\Delta \ell_r$ (cm)	$\Delta \ell_c$ (cm)	Δt (s)	$\overline{V}_i$ (cm/s)	$\overline{V}_f$ (cm/s)	$\overline{V}_f$ (cm/s)	$\overline{V}_r/\overline{V}_f$
52	20.64	4.28	5.39	401	2.58	6.52	1.37	0.210
53	20.64	4.36	5.14	416	2.47	6.29	1.34	0.213
54	21.11	4.44	5.39	418	2.52	6.39	1.36	0.213
55	15.72	0	5.14	413	2.40	2.40	0	0
56	28.41	11.27	5.51	421	2.57	8.57	3.42	0.400
57	28.26	11.27	5.23	437	2.45	8.21	3.30	0.402
58	28.73	11.19	6.36	418	2.65	8.73	3.42	0.392
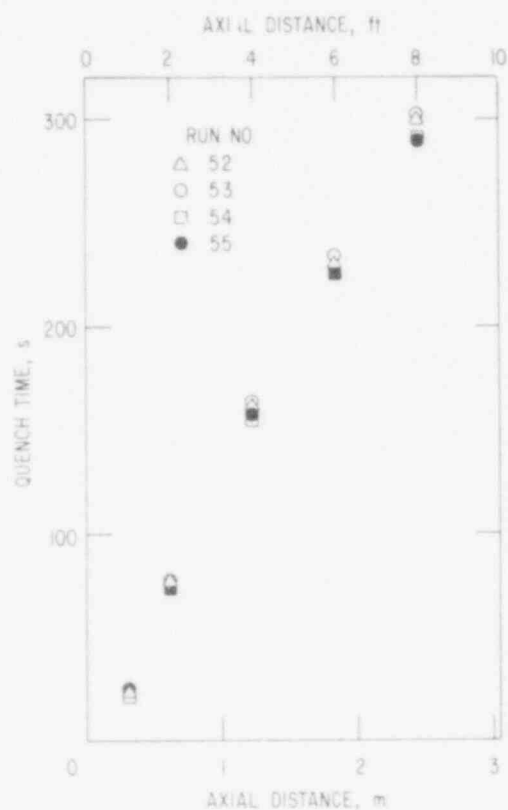
Fig. I.18

Quench Time vs Axial
Distance for Runs 52–55.
ANL Neg. No. 900-79-59.

Figure I.18 compares the quench
time and axial distance for Runs 52-55. The
differences in quench time at the same axial
distance are small (less than 5%). The quench
time at a given axial location appears to de-
crease slightly with increasing frequency of
oscillation. These observations agree with
those tests conducted with the solenoid valve
system for the same inlet average velocity.

As shown in Tables I.4 and I.5,
Runs 56-58 were performed with pressure in
the receiving tank less than the atmospheric
pressure; this increased the mean velocity for
the reverse flow as compared to Runs 52-54.
Thus, Runs 56-58 have a velocity ratio
($\overline{V}_r/\overline{V}_f$) nearly twice that of Runs 52-54, even
though they both have approximately the same
inlet average velocity to the test section ($\overline{V}_i$).
Figures I.17-I.21 compare quench times and
axial distances between Runs 52 and 56,
53 and 57, and 54 and 58. Increasing the mag-
nitude of the reverse flow is seen to slow down
the quench process slightly. However, the
difference is again seen to be small in the
range of variables tested.
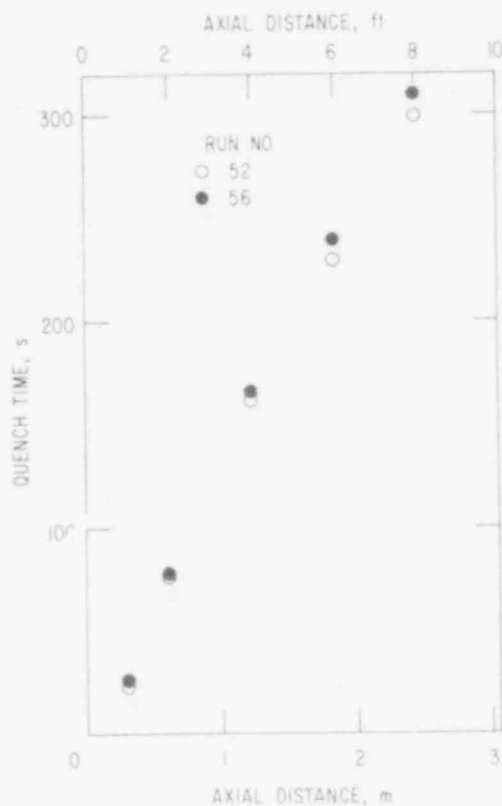
Fig. I.19

Quench Time vs Axial Distance
for Runs 52 and 56. ANL Neg.
No. 900-79-57.

18
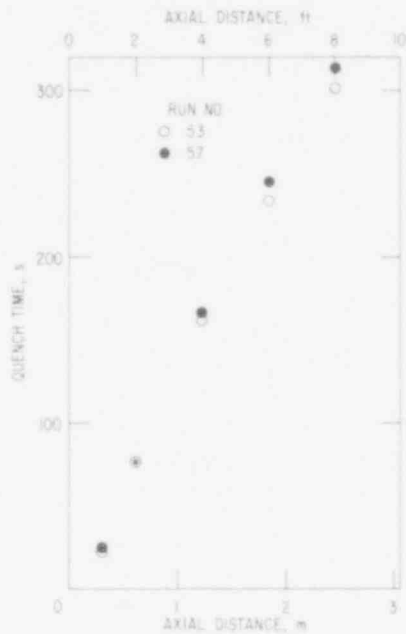
Fig. I.20. Quench Time vs Axial
Distance for Runs 53
and 57. ANL Neg.
No. 900-79-56.
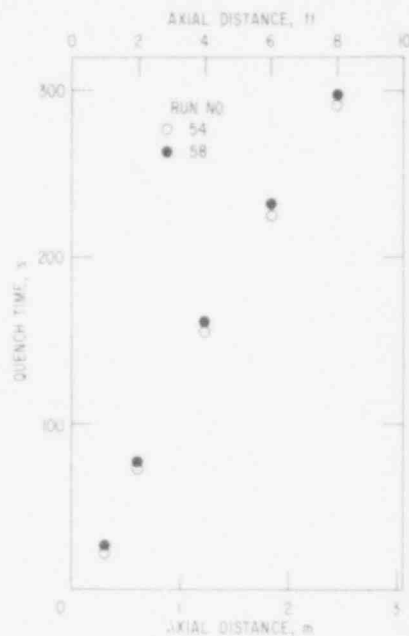
Fig. I.21. Quench Time vs Axial
Distance for Runs 54
and 58. ANL Neg.
No. 900-79-61.

References

1. J. C. M. Leung and R. E. Henry, "Transient Critical Heat Flux," Light-water-reactor Safety Research Program: Quarterly Progress Report, January-March 1978 ANL-78-49, NUREG/CR-0201, pp. 1-27 (July 1978).

2. M. Cumo, G. Ferrari, and G. Urbani, "Prediction of Burnout Power with Freon Up to the Critical Pressure," European Two-Phase Group Meeting, Casaccia, Rome (June 6-8, 1972).

3. J. G. Collier, Convective Boiling and Condensation, Chapter 9, McGraw-Hill Book (1972).

4. D. H. Lee and J. D. Obertelli, An Experimental Investigation of Forced Convection Boiling in High Pressure Water, Part 1, AEEW-R213 (1963).

5. R. T. Lahey and J. M. Gonzalez-Santalo, "The Effect of Non-uniform Axial Heat Flux on Critical Power," Proc. Heat and Fluid Flow in Water Reactor Safety Meeting, Manchester, p. 193 (1977).

6. L. S. Tong, Prediction of Departure from Nucleate Boiling for an Axially Non-uniform Heat Flux Distribution, J. Nucl. Energy 21, 241 (1967).

7. M. Silvestri, On the Burnout Equation and on Location of Burnout Points, Energ. Nucl. 13, 469 (1966).

8. D. H. Lee, An Experimental Investigation of Forced Convection Burnout in High Pressure Water: Part III. Long Tubes with Uniform and Non-uniform Axial Heating, AEEW-R355 (1965).

9. J. C. M. Leung and R. E. Henry, unpublished ANL report (1978).

II. TRANSIENT FUEL RESPONSE AND FISSION-PRODUCT RELEASE PROGRAM

Principal Investigators
J. Rest and S. M. Gehl, MSD

A. Introduction and Summary

A physically realistic description of fuel swelling and fission-gas release is needed to aid in predicting the behavior of fuel rods and fission gases under certain hypothetical light-water-reactor (LWR) accident conditions. To satisfy this need, a comprehensive computer-base model, the Steady-state and Transient Gas-release and Swelling Subroutine (GRASS-SST), is being developed at Argonne National Laboratory (ANL). This model is being incorporated into the Fuel-rod Analysis Program (FRAP) code being developed by EG&G Idaho, Inc., at the Idaho National Engineering Laboratory (INEL).

The analytical effort is supported by a data base and correlations developed from characterization of irradiated LWR fuel and from out-of-reactor transient heating tests of irradiated commercial and experimental LWR fuel under a range of thermal conditions.

Emphasis in the early stages of the program has been on thermal conditions in pressurized-water-reactor (PWR) fuel that are applicable to anticipated hypothetical power-cooling-mismatch (PCM) accidents. Recent efforts include conditions typical of other types of hypothetical accidents. The program is also developing information on fission-gas release during steady-state and load-following operations.

Recent significant experimental and analytical advances at the end of this quarter are summarized below:

1. Quantitative stereology measurements have been completed on four PCM simulations in the high-heating-rate series. High heating rates alter the relationship between fission-gas release and transient microstructural change.

2. The replacement DEH chamber is ~50% complete.

3. Models describing the evolution of the bubble-size classes in FASTGRASS have been developed and implemented into the code. Initial runs for steady-state and DEH test conditions indicate that FASTGRASS-calculated fission-gas release is in reasonable agreement with the experimental measurements.

4. Qualitative differences between the predicted and experimental results for the radial profile of transient fission-gas release indicate that the

GRASS model for the rapid, long-range interconnection of grain-edge porosity is too simple to account for the evolution of the grain-edge porosity observed in DEH-tested fuel.

J. Rest and S. M. Gehl attended the Fuel Code Program Review on October 4, 1978, in Silver Spring, Maryland, and gave a presentation titled "The GRASS Computer Code and DEH Testing at ANL."

B. Modeling of Fuel/Fission-product Behavior (J. Rest, MSD)

1. Development of FASTGRASS, A Fast-running Option to GRASS-SST

a. Introduction

The most important differences between FASTGRASS and GRASS-SST are in the algorithms used for calculating the evolution of bubble density and size over time. In GRASS-SST, the bubble-size distribution is specified by calculating the densities of bubbles in each of a number of bubble-size classes. Each bubble-size class is characterized by an average number of atoms per bubble, the value of which differs from that of the preceding size class by a constant multiplier. (The number of size classes is a variable that is determined dynamically during a computer run.) Changes in the bubble-size distribution, caused by bubble coalescence and re-solution, for example, are determined by solving a large number of integral-differential equations for each time step. Solutions are carried out for bubbles on grain surfaces, along dislocations, and in the bulk matrix. The iterative solution of a large number of coupled equations is a major contributor to the computer run times of GRASS-SST.

In contrast to the multiclass description of the bubble-size distribution in GRASS-SST, FASTGRASS uses only two classes: one for single gas atoms and one for gas bubbles. In addition, the description of bubbles on dislocations has been deleted. In GRASS-SST, the same delineation of bubble sizes in terms of the number of gas atoms per bubble is used for intergranular, intragranular, and dislocation bubbles. This is possible because enough size classes are available to fully characterize the distributions. In FASTGRASS, with only two size classes available for inter- and intragranular bubbles, separate descriptions of the size classes are necessary for the intragranular and grain-surface bubbles. The single gas atoms are characterized by their number density and atomic radius; the gas bubbles are characterized by number density and average size, expressed as the number of atoms per bubble. The number densities of atoms and bubbles are determined for both the intragranular and grain-surface regions by solving the set of equations

$$\frac{df_i}{dt} = -a_i f_i^2 - b_i f_i + c_i, \tag{1}$$

$$\frac{df_2}{dt} = -b_2 f_2 + c_2, \tag{2}$$

$$\frac{dg_1}{dt} = -A_1 g_1^2 - B_1 g_1 + C_1, \tag{3}$$

and

$$\frac{dg_2}{dt} = -B_2 g_2 + C_2, \tag{4}$$

where f_1 and f_2 are the single-atom and bubble densities, respectively, for the intragranular region, and g_1 and g_2 are the corresponding quantities for the grain boundaries. The other parameters were defined in ANL-78-77 (pp. 10-16). The parameters in Eqs. 1-4 are, in general, functions of the average bubble size, S. In ANL-78-77, S was assumed to have a constant value. However, any realistic calculation of gas-bubble behavior must account for changes in the average bubble size that may occur during irradiation.

Work this quarter has culminated in a model for calculating the evolution of S as follows: During each time step, the processes of bubble nucleation, gas-atom diffusion to bubbles, bubble coalescence, and bubble re-solution can lead to changes in the average bubble size. Coalescence increases S, while re-solution decreases S; bubble nucleation and gas-atom diffusion to bubbles tend to stabilize S. Let ξ be the fractional change in bubble density during a particular time step. Then

$$\xi = \frac{Fh}{y_2}, \tag{5}$$

where F is the rate at which the bubble density is changing as a result of the above-mentioned processes, $y_2 = f_2$ or g_2 is the bubble density, and h is the internal time step of the code (ξ does not depend on time-step selection, as F is also a function of h). If ξ is greater than a threshold value ϵ and bubble density is increasing, the bubble size is increased by a factor of δ. Similarly, if ξ is greater than ϵ and bubble density is decreasing, the average bubble size is decreased by a factor of δ. Note that a change in bubble size leads to a corresponding change in bubble density, since the total number of gas atoms in bubbles is conserved. The convergence parameters ϵ and δ were determined to have the values 0.05 and 5, respectively, by decreasing them to the point where further reductions had a minimal effect on calculated results.

b. Comparison of Code Predictions for Transient Gas Release with Experimental Results

The GRASS-SST and FASTGRASS codes were used to calculate fission-gas release for a series of DEH experiments. FASTGRASS

executed these problems approximately one order of magnitude faster than
GRASS-SST. The results of these calculations are shown in Figs. II.1 and II.2.
In each of these figures, the solid line indicates the position of perfect agree-
ment between predictions and experiment. As is evident, the GRASS-SST and
FASTGRASS predictions are in reasonable agreement with the experimental
measurements.
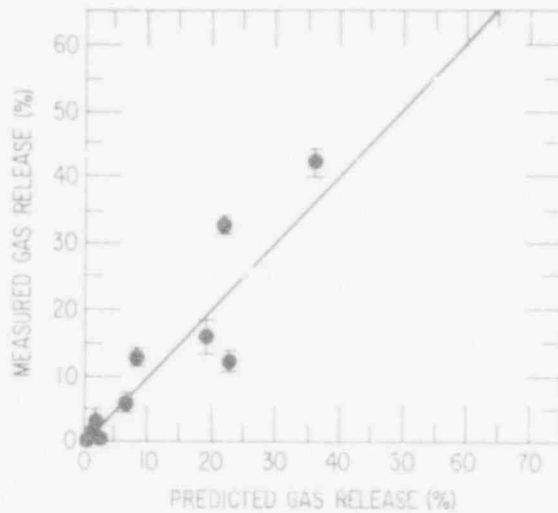
Fig. II.1. GRASS-SST-predicted Transient Gas
Release vs Experimentally Measured
Values. Neg. No. MSD-65943.
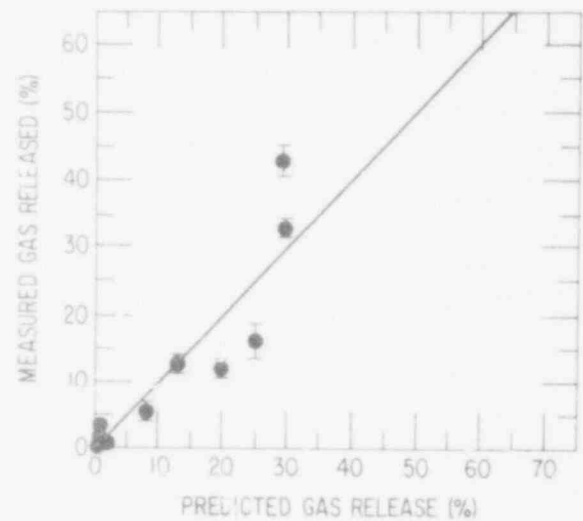
Fig. II.2. FASTGRASS-predicted Transient Gas
Release vs Experimentally Measured
Values. Neg. No. MSD-65942.
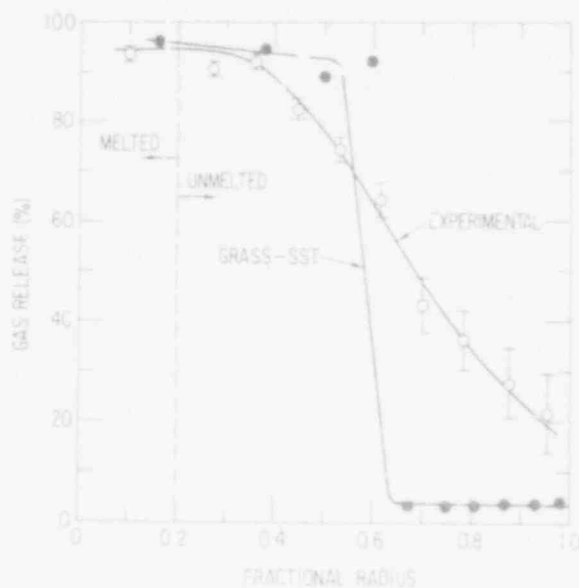
Fig. II.3. Radial Profiles of Fission-gas Release for
DEH Test 33. Neg. No. MSD-65944.

Figure II.3 shows GRASS-SST
results for the radial profile of transient
fission-gas (xenon) release during DEH
Test 33, plotted with laser-sampling data
for krypton. (The FASTGRASS predic-
tions are similar.) The predicted results
show a gradual decrease in fission-gas
release from 96% at a fractional radius
of 0.16 to about 90% at a fractional radius
of 0.69. The predicted release then de-
creases sharply in a stepwise manner to
about 4% for the rest of the radius. This
behavior is in contrast with the relatively
smooth decline in the fractional fission-
gas release from 82% at a fractional
radius of 0.48 to 20% at a fractional
radius of 0.90, as shown in Fig. II.3. The
area under the predicted curve is approx-
imately equal to the area under the ex-
perimental curve; this result is reflected
in the reasonable GRASS-SST prediction of total transient fission-gas release
(~40%) during Test 33, as shown in Fig. II.1.

c.   Discussion of Results

Figures II.1 and II.2 show that both GRASS-SST and
FASTGRASS give reasonable predictions of fission-gas release for a series
of DEH experiments that encompass a wide range of heating rates and maxi-
mum fuel temperatures. (In addition, FASTGRASS results for average bubble
size are in reasonable agreement with the GRASS-SST calculations of the
fission-gas bubble-size distribution.) Note that the predictions agree to within
a factor of two with the experimental values, and that the predictive capabilities
of GRASS-SST and FASTGRASS are roughly equal. Therefore, the greater com-
puting speed of FASTGRASS makes this code an attractive alternative for some
analytical descriptions of fuel-rod behavior. On the other hand, GRASS-SST
is useful for applications in which more detailed predictions, e.g., bubble-size
distributions, are necessary, and for substantiating FASTGRASS predictions
for specific conditions of interest.

The differences between the predicted and measured fission-
gas release values in Figs. II.1 and II.2 are the summation of several contrib-
uting effects. The following discussion of possible sources of error is not
meant to be exhaustive. Rather, the intent is to illustrate some of the problems
that have been encountered in using the GRASS-SST and FASTGRASS models.

Inaccuracies in the measurement of the fission gas released
during the DEH transients lead to an uncertainty of up to 5% in the reported
values. These uncertainties are indicated in Figs. II.1 and II.2. Uncertainties
in the calculated transient temperatures used by GRASS-SST and FASTGRASS
can lead to additional errors. These uncertainties are due to the approxima-
tions used in estimating the high-temperature thermal and electrical conduc-
tivities and the experimental error in surface-temperature measurement.

Another source of the differences shown in Figs. II.1 and II.2
is the oversimplified nature of the pore-interlinkage model used in GRASS-SST
and FASTGRASS. This model is based on the assumption that rapid long-range
interconnection of the grain-edge porosity occurs when the grain-edge gas-
bubble fractional swelling exceeds 5%. Thus, the stepwise decrease in the pre-
dicted release at a fractional radius of 0.69 in Fig. II.3 is due to the transition
from fuel regions where the gas-bubble swelling was greater than 5% (for
fractional radii less than 0.65) to fuel regions where the swelling was less than
5% (for fractional radii greater than 0.65).

The qualitative difference between the predicted and experi-
mental results for the radial profile of transient fission-gas release (and,
calculations indicate, some of the deviation of the predicted gas release from
the measured results shown in Figs. II.1 and II.2) indicates that the GRASS-SST
and FASTGRASS models for the rapid, long-range interconnection of grain-edge
porosity are too simple to account for the evolution of the grain-edge porosity ob-
served in DEH-tested fuel. A more realistic calculation of the radial profile of

transient fission-gas release would have to include models describing the evolution of the intergranular porosity as a function of the gas-bubble distribution, the temperature and heating rate, the fuel microstructure, and the local stresses generated within the fuel pellet. This work is currently in progress.

C. Experimental Program (S. M. Gehl, MSD)

1. Microstructural Characterization of DEH-tested Fuel

Quantitative stereology measurements of the pore volume fraction, V_v, and pore-solid surface area, S_v, were completed for the fuel specimens from the series of DEH tests performed at high heating rates. (See ANL-78-49, pp. 39-40, for a description of these tests.) The changes in V_v and S_v from their pretest values were used to calculate the volume swelling and the increase in pore-solid surface area per gram of fuel, S_g. The parameters V_v, S_v, swelling (as a percent of the pretest fuel volume), and S_g are reported in Table II.1.

TABLE II.1. Summary of Microstructural Examination Results for DEH Tests at High Heating Rates

Test No.	Fractional Melt Radius	Xenon Release, %	Xenon Release from Solid,[a] %	V_v	Swelling %	S_v, mm^{-1}	S_g, mm^{2}g^{-1}
37	0	5.9	5.9	0.093	6.9	224	1.60 $\times 10^4$
38	0.38	33.7	23	0.127	11.1	264	2.11 $\times 10^4$
39	0.47	44.0	28	0.274	33.6	447	4.97 $\times 10^4$
40	0.38	36.2	26	0.182	18.6	334	3.07 $\times 10^4$

[a]Assuming 100% release from the melted fuel.

The radii of the melt zones (expressed as a fraction of the pellet radius) are also reported in Table II.1 for those tests in which melting occurred. The fractional fission-gas release for the fuel that did not melt is also given in Table II.1. This parameter is calculated by assuming a 100% gas release from the melted fuel. Laser sampling of the melted fuel from the Test 33 specimen indicates that this assumption is a good approximation. (See ANL-78-25, pp. 16-19, for a description of the laser-sampling results.)

2. Development of Empirical Correlations for Transient Fission-gas Release

Empirical correlations for fission-gas release are being sought in two areas: (1) correlations of gas release with the thermal history of PCM-type transients, and (2) correlations of gas release with transient-induced microstructural changes. The dependence of fission-gas release on temperature parameters was discussed in ANL-78-107. The present report discusses recent work on the relationships between gas release and microstructural change.

The initial series of PCM-type tests exhibited strong correlations between fission-gas release and the formation of intergranular separations during transient heating.[1] One important feature of these correlations was that a rapid increase in fission-gas release was observed when a "critical" amount of microstructural change had occurred. The critical values of swelling and S_g were 18% and 2.5×10^4 mm^2/g, respectively.[1] The existence of critical values of microstructural change was tentatively ascribed to the onset of inter-linkage of the intergranular porosity and venting of the entrained fission gas. Subsequent tests in which the fuel-center heating rate was between 10 and 50 K/s followed the pattern exhibited by the initial test series.

However, the series of high-heating-rate DEH tests deviate signif-icantly from the behavior observed previously, as shown in the graph of xenon release as a function of S_g (Fig. II.4). The xenon-release values report only the gas released from the unmelted portions of the specimens. A similar graph is obtained when xenon-release is plotted against volume swelling. The solid line in Fig. II.4 follows the data of the lower-heating-rate tests; the dashed line indicates the probable behavior of the high-heating-rate tests. Note, however, that the results for the higher heating rates are tentative and may change as more data become available.

The most important difference between the two sets of data is that xenon release appears to reach a saturation value of ~30% for the higher heating rates; at lower heating rates, a saturation behavior either does not occur or occurs only for gas-release fractions in excess of 60%. In this context, saturation means that, beyond a certain point, additional microstruc-tural change has a negligible effect on gas release. Future tests in the high-heating-rate series will be designed to further investigate the saturation effect and its potential for providing an upper limit in gas release during PCM transients.

Fig. II.4. Xenon Release as a Function of Microcrack Surface Area for DEH-tested Specimens. Neg. No. MSD-66172.

3. Replacement DEH Test Chamber (S. M. Gehl and D. R. Pepalis, MSD)

The design of the replacement DEH test chamber has been completed, and fabrication of the chamber in the ANL machine shops is ~50% complete. Fabrication will be completed, the equipment will be assembled, and its operation will be checked in the coming quarter.

Reference

1. S. M. Gehl, M. G. Seitz, and J. Rest. Fission-gas Release from Irradiated PWR Fuel during Simulated PCM-type Accidents: Progress Report, ANL-77-80, NUREG/CR-0088 (May 1978).

III. MECHANICAL PROPERTIES OF ZIRCALOY

H. M. Chung, A. M. Garde, and T. F. Kassner, MSD

A. Summary

Since hydrogen uptake as well as oxidation can occur at the inner surface of Zircaloy cladding after deformation and rupture of internally pressurized tubes in steam, the effect of hydrogen on the instrumented-impact properties of Zircaloy is being evaluated. The experimental methods and dimensions of the subsize-Charpy specimens are the same as those used to determine the impact properties of Zircaloy-oxygen alloys. Information on the maximum load, dynamic fracture toughness, and total absorbed energy was obtained at temperatures between 373 and 823 K for homogeneous alloys with ~10-1300 ppm hydrogen. The results indicate that ~600-1300 ppm hydrogen in Zircaloy has a significant effect on the dynamic fracture toughness at temperatures ≲600 K.

The diametral ring-deflection properties of undeformed Zircaloy cladding, which was oxidized on the inner and outer surfaces in steam at temperatures between ~1350 and 1700 K, have been correlated with pendulum-impact results obtained from the identical tubes. The load-versus-deflection curves provide information on the plastic deformation to the point of an initial crack as well as total deflection to fragmentation of the ring segment. The deflection values range from ~0 to 0.4 and 0.2 to 1.2 mm, respectively, for failure-impact energies between ~0.02 and 0.5 J at 300 K.

Several Zircaloy cladding specimens from integral tube-burst/ thermal-shock tests were sectioned at several axial positions for metallographic evaluation of oxide-layer thickness and for chemical analysis of hydrogen. The results indicate that hydrogen pickup by the tubes during oxidation in steam occurred primarily in regions where the inner-surface oxide layer was either quite thin or in locations where a relatively thick porous oxide formed. The hydrogen content of the Zircaloy cladding varied between ~25 and 2000 ppm.

The information obtained for the thermal-shock, impact, and ring-deflection properties of Zircaloy containing oxygen and hydrogen will be used to establish an embrittlement criterion applicable to fuel cladding under hypothetical LOCA situations.

B. Impact Properties of Zircaloy-Hydrogen Alloys

Hydrogen uptake occurs at the inner surface of Zircaloy cladding after deformation and rupture of internally pressurized tubes in steam and oxidation at temperatures between ~1200 and 1400 K.[1-4] Consequently, hydrogen as well as oxygen may influence the mechanical properties of the cladding at

temperatures encountered in the later stage of a hypothetical LOCA transient (i.e., ≤600 K). Kawasaki et al.[1] have shown that the ductility of Zircaloy cladding, as determined by diametral ring-compression measurements at 373 K, is quite small (i.e., ≤1.0 mm) when the hydrogen content is ≥250 ppm. Since impact behavior of Zircaloy is relevant to the development of embrittlement criteria for fuel cladding, the effect of hydrogen on the instrumented-impact properties of Zircaloy is being evaluated for comparison with previously reported results[5,6] for homogeneous Zircaloy-oxygen alloys.

The specimen geometry and experimental methods are the same as those used in the impact measurements on Zircaloy-oxygen alloys;[7] however, the subsize-Charpy specimens were charged with hydrogen and homogenized in hydrogen-helium gas mixtures at temperatures of 1198 and 1223 K. The time-temperature conditions are given in Table III.1 along with hydrogen concentrations of the specimens, which were determined from weight-gain data and confirmed by chemical analyses. The specimens, which also contained ~1300 ppm oxygen, were cooled through the β → α phase transformation at ~0.3 K/s.

TABLE III.1. Hydrogen-charging and Homogenization Conditions for Zircaloy-2 Subsize-Charpy Impact Specimens[a]

Charging and Homogenization Temperature, K	Initial Pressure of H_2 and He, kPa	Time, ks	Hydrogen Content, wt ppm
1198	4.0 (H_2) 66.6 (He)	3.6	600
1198	11.2 (H_2) 63.3 (He)	10.8	760
1223	13.6 (H_2) 56.7 (He)	5.4	940
1198	8.0 (H_2) 66.6 (He)	5.4	1000
1198	10.0 (H_2) 63.3 (He)	5.4	1200
1223	20.0 (H_2) 53.3 (He)	5.4	1330

[a] 5 mm wide x 5 mm thick x 55 mm long with a longitudinal texture; i.e., long dimension is parallel to the rolling direction of the plate.

Information on the maximum load, dynamic fracture toughness, and total absorbed energy was obtained as a function of hydrogen content at several temperatures between 373 and 673 K. For an impact velocity of 0.75 m/s, Fig. III.1 shows the dependence of maximum load on hydrogen content. The maximum load is not strongly dependent on temperature and is independent of the hydrogen content for values ≥600 ppm (i.e., ~0.75 ± 0.1 kN). Figure III.2 shows the dependence of the dynamic fracture toughness on hydrogen content. The fracture toughness decreases as the hydrogen concentration increases at

all temperatures; however, for temperatures ≤ 573 K and hydrogen concentrations ≥ 600 ppm, the toughness values are quite low (~ 10-15 MPa·m$^{1/2}$). Scanning-electron micrographs of the fracture surfaces of specimens tested under these conditions (e.g., Fig. III.3) reveal a predominantly brittle fracture mode, whereas at 673 K, the specimens with fracture-toughness values ≥ 40 MPa·m$^{1/2}$ fail in a ductile manner.

Figures III.4 and III.5 show the effect of hydrogen concentration and temperature on the total absorbed energy per unit area. Except for the as-received material (1300 ppm oxygen and 10 ppm hydrogen), all specimens exhibited a predominantly brittle fracture mode.

Since the solubility of hydrogen in α-Zircaloy is quite low[8,9] (e.g., ~ 300 and 100 ppm at 673 and 573 K, respectively), most of the hydrogen in the impact specimens is present in the form of the hydride phase. Figure III.6 is a micrograph of a Zircaloy specimen (1000 ppm hydrogen and 1300 ppm oxygen), which was slow-cooled through the $\beta \rightarrow \alpha$ phase transformation. In contrast to oxygen redistribution during cooling through the phase transformation,[10] hydrogen concentrates at the periphery of the α plates; i.e., the central region
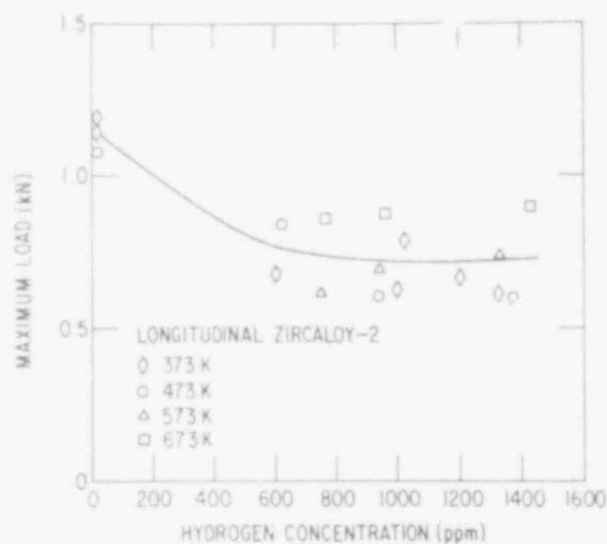
Fig. III.1. Maximum Load as a Function of Hydrogen Concentration of Homogeneous Zircaloy-2 Specimens at Several Temperatures between 373 and 673 K. Neg. No. MSD-65979.
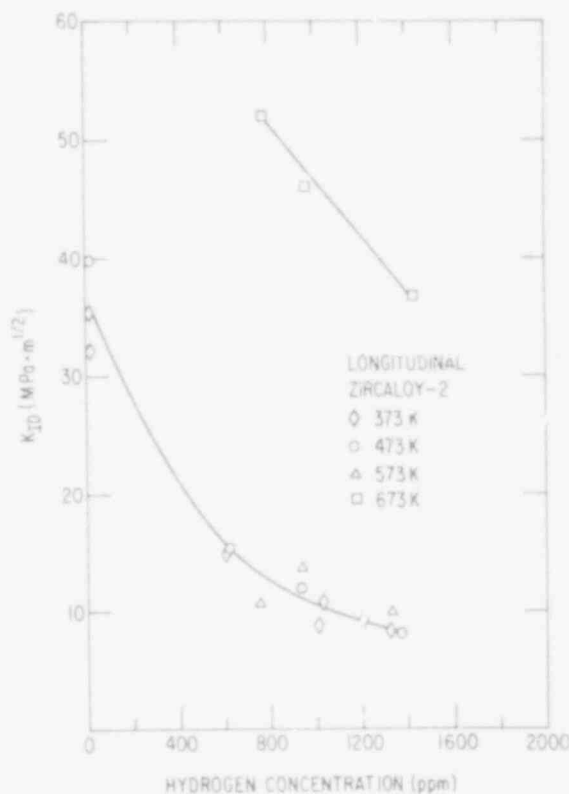
Fig. III.2. Dynamic Fracture Toughness of Homogeneous Zircaloy-2 Specimens as a Function of Hydrogen Concentration at Several Temperatures between 373 and 673 K. Neg. No. MSD-65967.

479 035

40 μm (a)

40 μm (b)
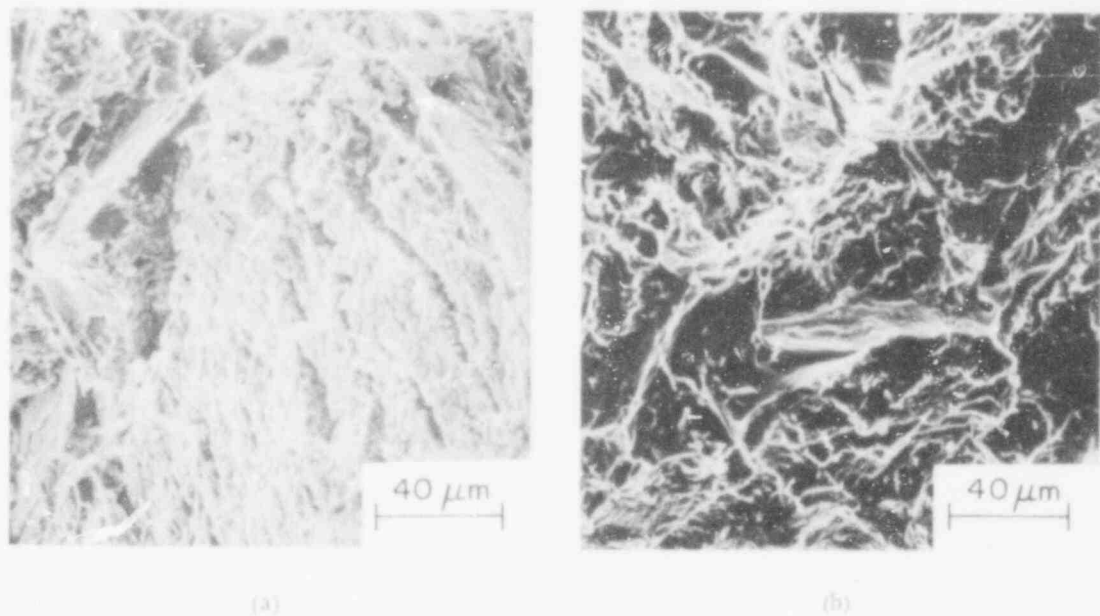
Fig. III.3. SEM Fractographs of Longitudinal Zircaloy-2 Specimens with 600 ppm Hydrogen Which Were Fractured by Impact at (a) 373 and (b) 473 K. The micrographs are indicative of a predominantly brittle fracture mode. Neg. Nos. MSD-66000 and -65998.
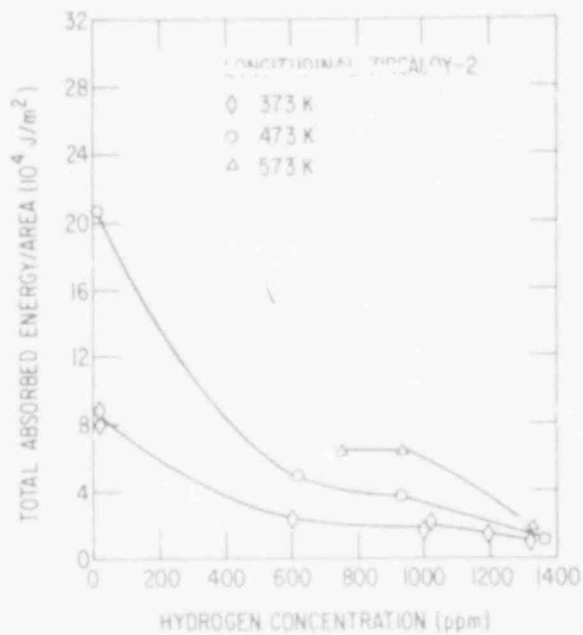
Fig. III.4. Total Absorbed Energy per Unit Area as a Function of Hydrogen Concentration of Homogeneous Zircaloy-2 Specimens at Temperatures of 373, 473, and 573 K. Neg. No. MSD-65973.
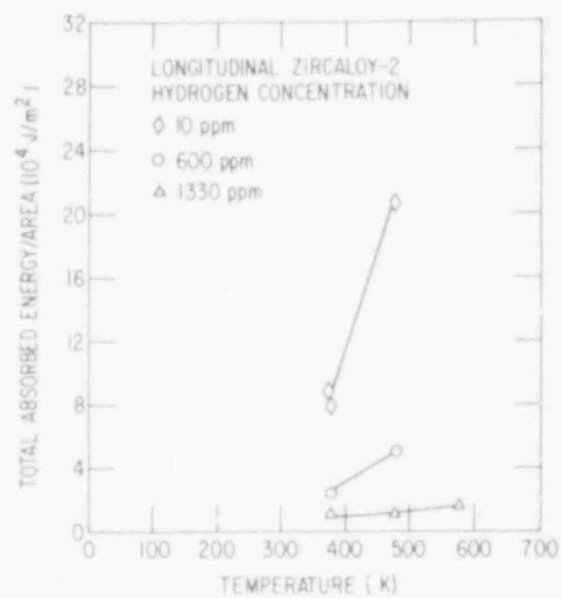
Fig. III.5. Total Absorbed Energy per Unit Area as a Function of Temperature for Homogeneous Zircaloy-2 Alloys with ~10, 600, and 1330 ppm Hydrogen. Neg. No. MSD-65981.
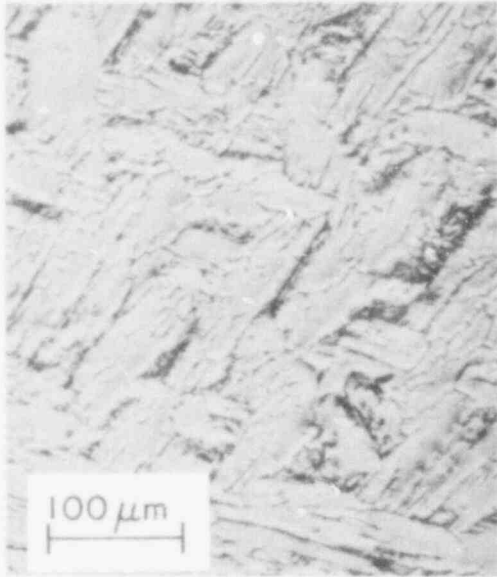
Fig. III.6

Optical Micrograph of a Zircaloy-2 Specimen
with 1000 ppm Hydrogen Which Shows Hydride
Precipitation at the Periphery of the α Plates.
The specimen was cooled through the β → α
phase-transformation region at ~0.3 K/s. Neg.
No. MSD-66001.

of the α plates appears to be relatively free of hydride precipitate. This
observation coupled with information on the ductile-to-brittle transition for
Zircaloy-oxygen (e.g., Figs. III.1 and III.3 of Ref. 6) and Zircaloy-hydrogen
(Fig. III.2) alloys suggests that a synergistic effect of oxygen and hydrogen on
the impact properties of Zircaloy may result for concentrations ≤4000 and
600 ppm, respectively, at temperatures ≤600 K. At low temperatures, higher
concentrations of either element result in a dynamic toughness value of
~10 MPa·m$^{1/2}$ and a total absorbed energy per unit area of ~2 x 10^4 J/m^2.
These values were used to establish impact-failure criteria for Zircaloy-
oxygen alloys relative to the oxygen concentration of the material and
temperature.[5,10]

The results on the instrumented-impact properties of Zircaloy-oxygen
and Zircaloy-hydrogen alloys, and information on the room-temperature im-
pact properties of Zircaloy-4 cladding after rupture and oxidation in steam
will be considered in the development of embrittlement criteria applicable to
fuel cladding under hypothetical LOCA conditions in LWR's.

C. Diametral Ring-compression and Impact-failure Properties of Undeformed Zircaloy-4 Cladding after Oxidation in Steam

The impact properties of undeformed Zircaloy-4 cladding, which was
oxidized on the inner and outer surfaces in steam at temperatures between
~1370 and 1680 K for various times and cooled to 300 K at a rate of ~5 K/s,
were reported previously.[6] To obtain a quantitative correlation between the
impact-failure and diametral ring-deflection properties at 300 K, we cut
6.35-mm-long segments from the tubes adjacent to the impact-fracture loca-
tion. The cladding segments were compressed at 300 K in an Instron testing
machine at a crosshead speed of 0.0423 mm/s. A typical load-versus-
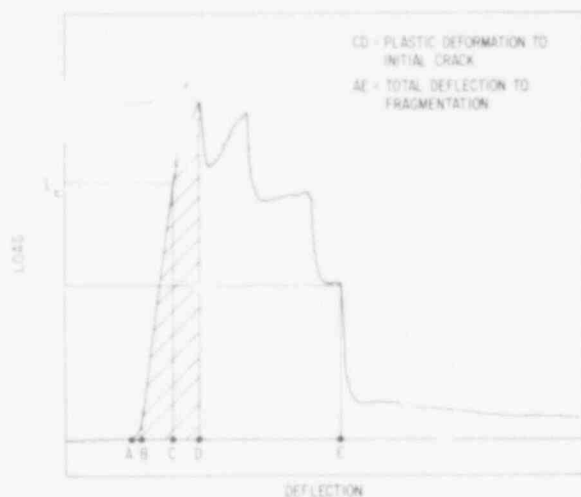deflection curve is shown in Fig. III.7. The deflection CD corresponds to the

Fig. III.7

Schematic of Typical Load-vs-Deflection Curve from a Diametral Ring-compression Test on a Segment of Oxidized Zircaloy Cladding. Abrupt decreases in load correspond to four sequential fractures before fragmentation during slow compression. ANL Neg. No. 306-79-75.

amount of plastic deformation to form the initial crack. As indicated by the abrupt decreases in the load, several additional fractures occur before fragmentation of the specimen at a total deflection denoted by AE on the figure.

Figure III.8 shows the plastic deformation to the point of the initial crack and the total deflection to fragmentation as a function of the failure-impact energy, which was obtained from the same tube. An impact energy of 0.3 J, which is a factor of 10 greater than the failure-impact energy for cladding that survives thermal-shock loading by a small margin,[5,11] corresponds to a plastic deflection of ~0.1 mm for the formation of an initial crack and to a total deflection of ~0.6-1.1 mm for fragmentation. The deflection to fragmentation is directly proportional to the failure-impact

energy. The ring-deflection tests on oxidized cladding that was slow-cooled through the $\beta \to \alpha'$ phase transformation are similar to those of Hobson,[12] which were performed on water-quenched specimens.

Fig. III.8

Plastic Deformation to Initial Crack and Total Deflection to Fragmentation (CD and AE, respectively, in Fig. III.7) as a Function of Failure-impact Energy at 300 K for Oxidized Zircaloy-4 Cladding. The inner and outer surfaces of the undeformed tubes were oxidized in steam at 1350-1700 K for various times and cooled through the $\beta \to \alpha'$ phase transformation at ~5 K/s. ANL Neg. No. 306-79-59.
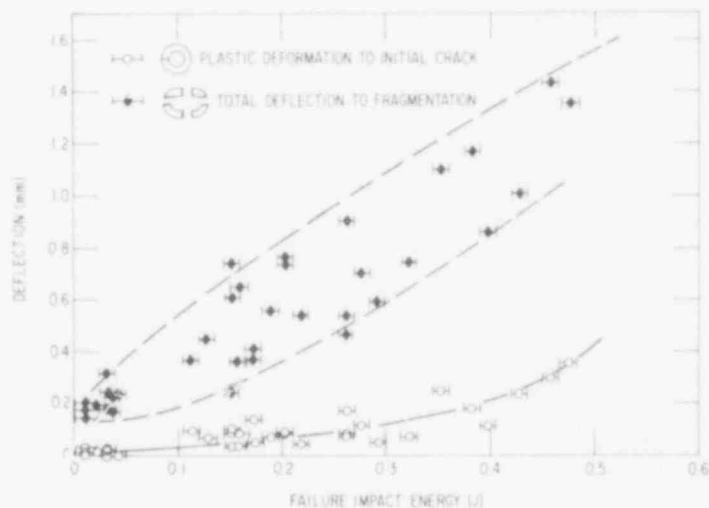
Figures III.9 and III.10 show the maximum load (L_M in Fig. III.7) and total deflection during ring compression at 300 K as a function of the transformed β-layer thickness of specimens oxidized on the inner and outer surfaces in steam at temperatures between 1373 and 1673 K. The load and deflection curves increase markedly for β-layer thicknesses larger than 0.25, 0.3, 0.35, and 0.4 mm for oxidation temperatures of 1373, 1477, 1588, and

1673 K, respectively. The failure-impact energy exhibited a similar dependence on the thickness of the transformed-β layer (i.e., Fig. III.20 of Ref. 6).
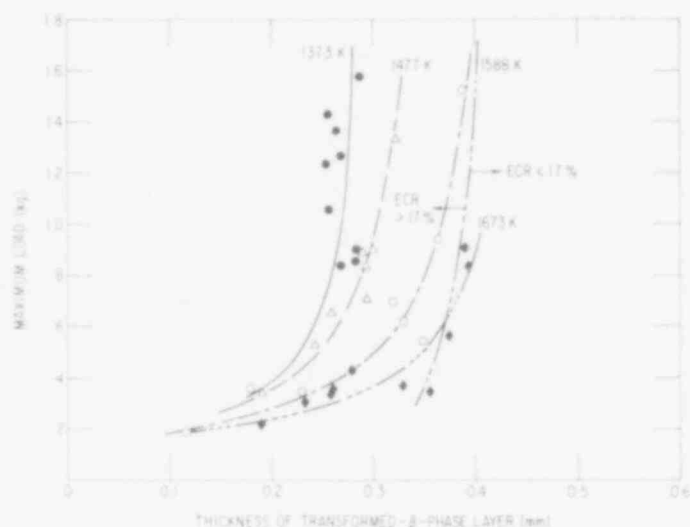

Fig. III.9

Maximum Load at 300 K as a Function of Thickness of Transformed β-phase Layer for 6.35-mm-long Segments of Undeformed Zircaloy-4 Cladding Oxidized in Steam at Inner and Outer Surfaces at 1373, 1477, 1588, and 1673 K and Cooled through the β → α' Phase Transformation at ~5 K/s. Ring-compression rate was 0.0423 mm/s. ANL Neg. No. 306-79-69 Rev.

Fig. III.10

Total Deflection to Fragmentation at 300 K as a Function of Thickness of Transformed β-phase Layer for 6.35-mm-long Segments of Undeformed Zircaloy-4 Cladding Oxidized in Steam at Inner and Outer Surfaces at 1373, 1477, 1588, and 1673 K and Cooled through β → α' Phase Transformation at ~5 K/s. Ring-compression rate was 0.0423 mm/s. ANL Neg. No. 306-79-67.
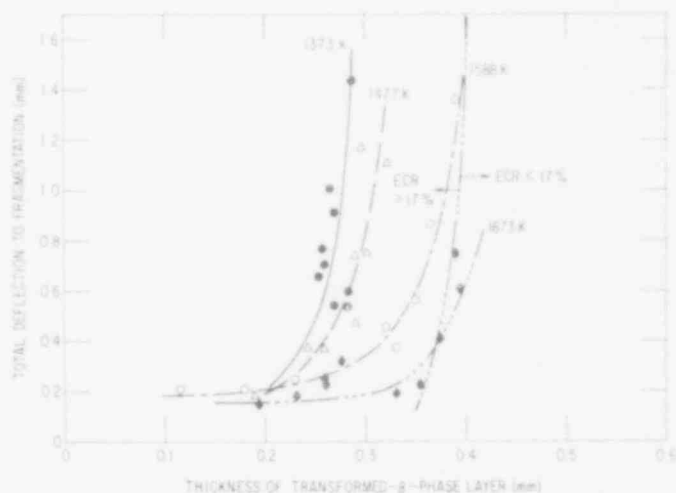
Based upon the measured oxide-, α-, and β-layer thicknesses, the amount of oxidation of the specimens was evaluated relative to the equivalent-cladding-reacted (ECR) parameter, which is used to define the 17% oxidation limit in the present cladding embrittlement criterion. The total deflection to fragmentation and the fracture-impact energy are plotted in Figs. III.11 and III.12, respectively, as a function of the equivalent-cladding-reacted parameter for undeformed Zircaloy cladding oxidized in steam at various temperatures.

These data show that, for undeformed cladding (i.e., no wall thinning due to deformation under internal pressure) in which a compact oxide layer forms on the inner and outer surfaces and hydrogen uptake is quite small (i.e., ≤ 60 ppm hydrogen in the tubes), the total deflection and failure-impact energy are relatively large (≥ 1.5 mm and ≥ 1.0 J) for cladding oxidized to the 17% ECR limit at temperatures ≤ 1600 K. As with the impact properties,[6] the

capability of deformed cladding to achieve a minimum specified deflection can be evaluated relative to the time and temperature of oxidation and the wall-thickness ratio that results from circumferential expansion of the cladding during transient heating and rupture.
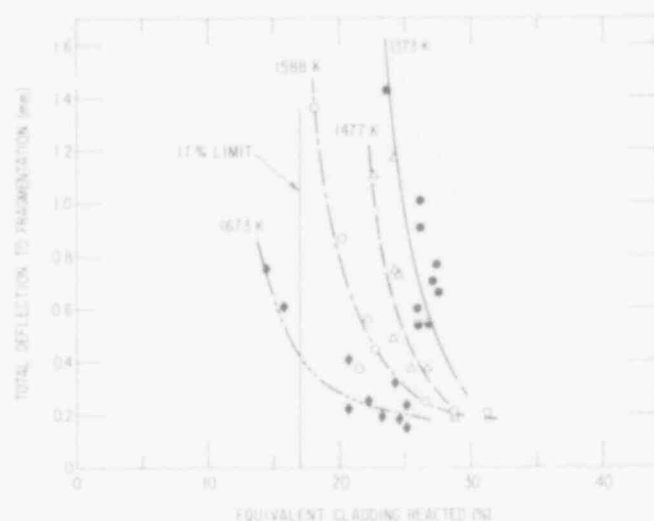

Fig. III.11. Relationship between Total Deflection to Fragmentation and Equivalent-cladding-reacted Parameter for Undeformed Zircaloy Cladding Oxidized in Steam at Inner and Outer Surfaces at 1373, 1477, 1588, and 1673 K and Cooled through $\beta \rightarrow \alpha'$ Phase Transformation at ~5 K/s. ANL Neg. No. 306-79-63.
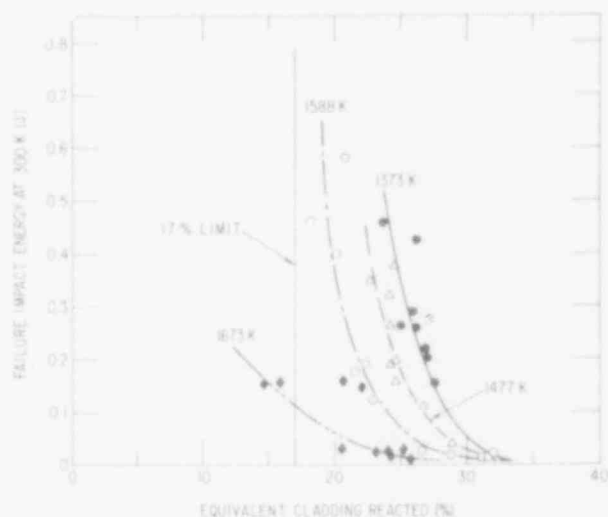
Fig. III.12. Relationship between Failure-impact Energy at 300 K and Equivalent-cladding-reacted Parameter for Undeformed Zircaloy Cladding Oxidized in Steam at Inner and Outer Surfaces at 1373, 1477, 1588, and 1673 K and Cooled through $\beta \rightarrow \alpha'$ Phase Transformation at ~5 K/s. ANL Neg. No. 306-79-66.

D. Correlation of Hydrogen Uptake and Inner-surface Oxidation of Zircaloy-4 Cladding from Integral Tube-burst/Thermal-shock Tests

Several specimens from the integral tube-burst/thermal-shock tests[5,7,13] have been sectioned at different axial locations and analyzed to assess the influence of hydrogen as well as oxygen on the room-temperature impact and ductility properties. Figure III.13 shows the time-temperature conditions for six tubes selected for correlation of the hydrogen content with inner-surface oxidation characteristics. The maximum axial temperature variation along the cladding is indicated in the figure; i.e., the temperature in ballooned regions is ~150-180 K lower than in adjacent nonballooned locations. The rupture opening in the tubes was ~80-150 mm², which is typical for Zircaloy cladding ruptured in the α- or predominantly α-phase region.[14]

Segments of the tube (~20 mm long) were analyzed for hydrogen, and adjacent regions (~6.3 mm long) were mounted and polished for metallographic determination of the morphology and thickness of the inner-surface oxide. The average hydrogen content and oxide-layer thickness are plotted as a function of axial position along the tube in Figs. III.14-III.19. The rupture location and the nature of the inner-surface oxide (porous versus compact) are also indicated in the figures.
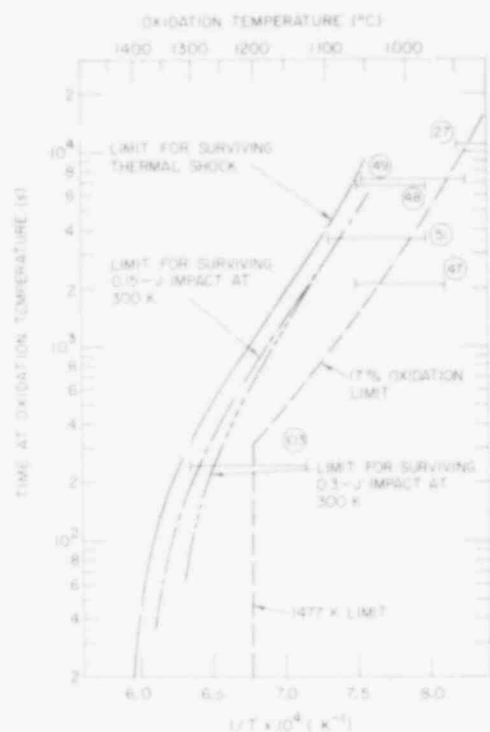
479 040

Fig. III.13

Time and Temperature Conditions during Oxidation of Zircaloy Specimens from Integral Tube-burst/Thermal-shock Tests Which Were Selected for Correlation of Hydrogen Content with Inner-surface Oxidation. The axial temperature variation during oxidation (denoted by the bars) was determined by five to seven thermocouples spot-welded to the cladding. ANL Neg. No. 306-78-660 Rev. 2.
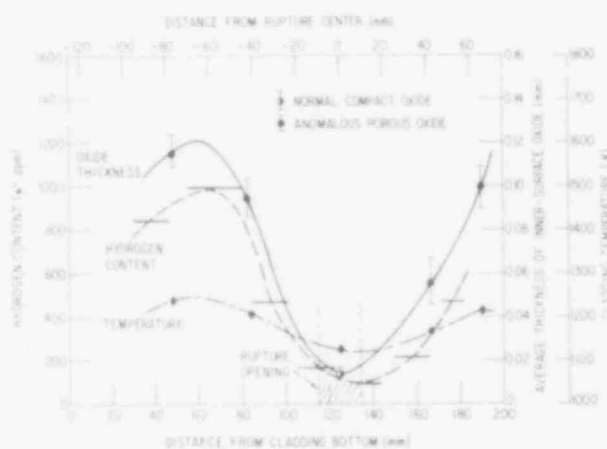

Fig. III.14. Hydrogen Content and Average Thickness of Inner-surface Oxide Layer as a Function of Axial Distance from Rupture Location of Zircaloy Tube Oxidized in Steam for 10.5 ks at 1120–1250 K. Tube No. 27 in Fig. III.13. ANL Neg. No. 306-79-73.
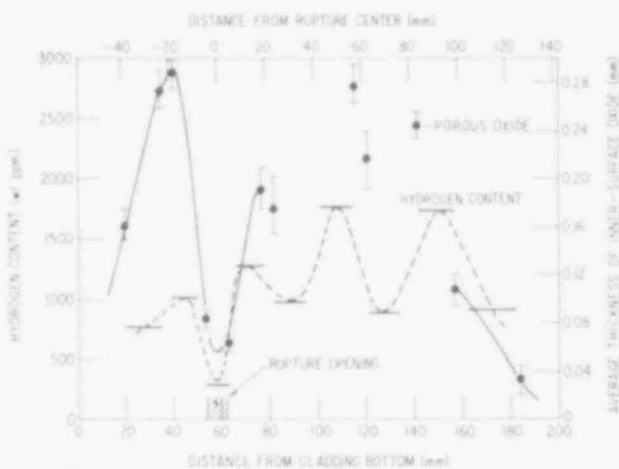
Fig. III.15. Hydrogen Content and Thickness of Inner-surface Oxide Layer as a Function of Axial Distance from Rupture Location of a Zircaloy Tube Oxidized in Steam for 7.2 ks at 1220–1330 K. Tube No. 49 in Fig. III.13. ANL Neg. No. 306-79-60.
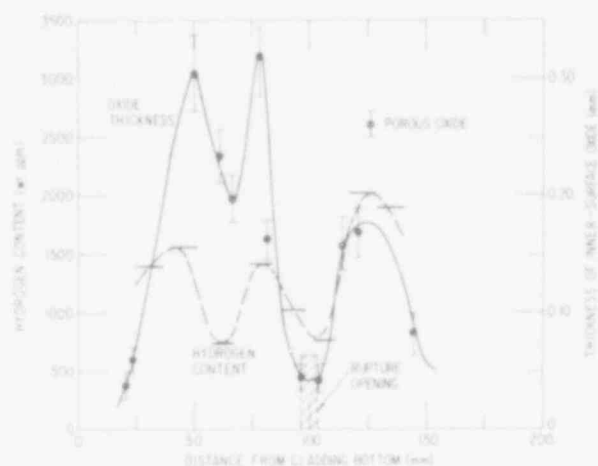
Fig. III.16. Hydrogen Content and Thickness of Inner-surface Oxide Layer as a Function of Axial Distance along Zircaloy Tube Oxidized in Steam for 7.0 ks at 1250–1350 K. Tube No. 48 in Fig. III.13. ANL Neg. No. 306-79-58.
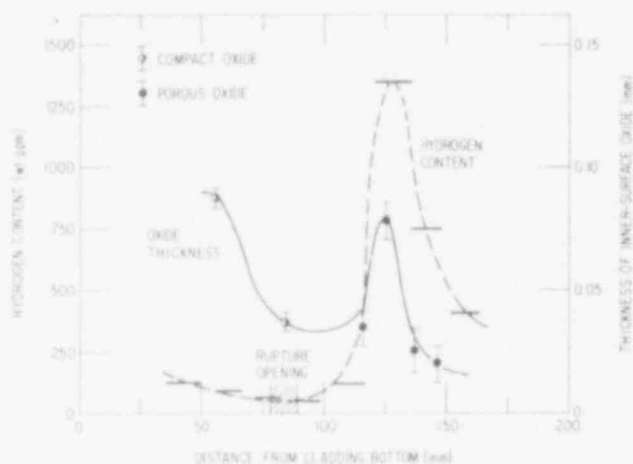
Fig. III.17. Hydrogen Content and Thickness of Inner-surface Oxide Layer as a Function of Axial Distance along Zircaloy Tube Oxidized in Steam for 3.6 ks at 1250–1380 K. Tube No. 51 in Fig. III.13. ANL Neg. No. 306-79-61.
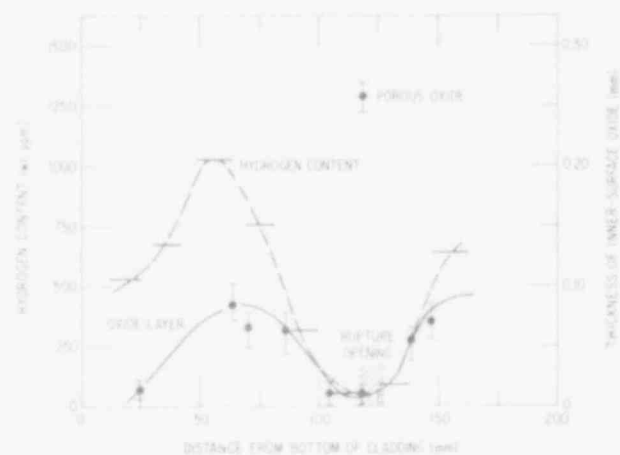
Fig. III.18. Hydrogen Content and Thickness of Inner-surface Oxide Layer as a Function of Axial Distance along Zircaloy Tube Oxidized in Steam for 2.1 ks at 1250–1335 K. Tube No. 47 in Fig. III.13. ANL Neg. No. 306-79-65.
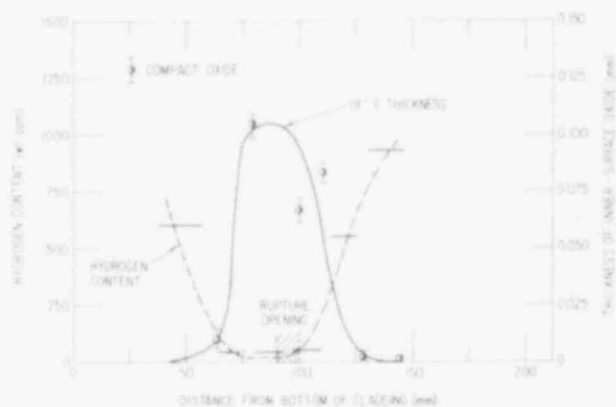
Fig. III.19. Hydrogen Content and Thickness of Inner-surface Oxide Layer as a Function of Axial Distance along Zircaloy Tube Oxidized in Steam for 0.24 ks at 1410–1580 K. Tube No. 103 in Fig. III.13. ANL Neg. No. 306-79-68.

Except for the tube that was oxidized at a relatively high temperature (i.e., 1410–1580 K, for tube No. 103 in Figs. III.13 and III.19) and the rupture locations in two tubes oxidized at ~1120–1380 K (i.e., tube Nos. 27 and 51 in Figs. III.14 and III.17, respectively), a porous oxide was observed on the inner surface. In a previous report (Fig. III.16 of Ref. 13), oxidation of ruptured cladding in steam at temperatures between 1170 and 1300 K for extended periods of time (~2 ks) resulted in the formation of porous oxide.

479 042

The information in Figs. III.14-III.18 indicates that hydrogen uptake by the cladding is directly proportional to the thickness of the porous oxide. In contrast, when the oxide layer is relatively thick and compact (e.g., ≥ 0.02 mm in Figs. III.17 and III.19), hydrogen uptake by the cladding is quite small (≤ 100 ppm); however, when the layer of compact oxide is negligibly thin (e.g., the region of the tube adjacent to the burst location in Fig. III.19), hydrogen uptake by the cladding is also large (≥ 600 ppm). Figure III.20 shows microstructures that illustrate the correlation between morphology of the inner-surface oxide and hydrogen uptake by the cladding.
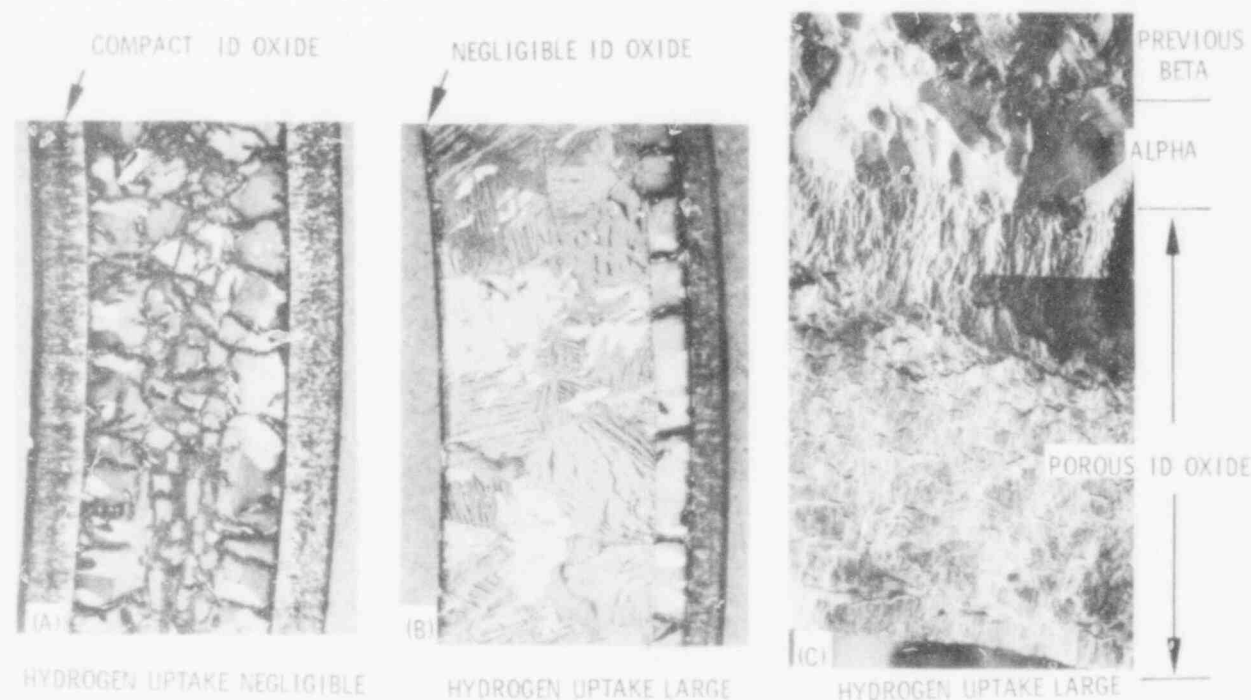

Fig. III.20. Microstructures of Cross Sections of Zircaloy Cladding from Integral Tube-burst/Thermal-shock Tests Illustrating Relationship between Thickness and Morphology (Compact vs Porous) of Inner-surface Oxide and Hydrogen Uptake by Cladding. ANL Neg. No. 306-78-220 Rev. 1.

A number of factors can influence the extent of Zircaloy cladding embrittlement by oxygen as well as hydrogen during oxidation in steam. Homma et al.[15] reported that the morphology of the oxide layer is primarily determined by the H_2/H_2O volume ratio; i.e., as the H_2/H_2O volume ratio increases, the oxide changes from compact → porous → negligibly thin film at temperatures between 1273 and 1373 K. Consequently, geometric factors (e.g., area of the rupture opening, pellet-cladding diametral-gap distance), local temperature, and axial temperature profile can influence hydrogen generation rate, dilution of hydrogen with steam, and uptake of hydrogen and oxygen at the inner surface of the cladding in regions away from the burst location.

References

1. S. Kawasaki, T. Furuta, and H. Uezuka, "Inner Surface Oxidation of Zircaloy Cladding in a Loss-of-Coolant Accident," Sixth Water-Reactor-Safety Research information Meeting, National Bureau of Standards, Gaithersburg, MD (Nov 6-9, 1978).

2. T. F. Kassner, H. M. Chung, A. M. Garde, and S. Majumdar, "Zircaloy Cladding Embrittlement, Recommended Criteria," Sixth Water-Reactor-Safety Research Information Meeting, National Bureau of Standards, Gaithersburg, MD (Nov 6-9, 1978).

3. S. Kawasaki, JAERI, private communication (Nov 13, 1978).

4. M. L. Picklesimer, "Comments on the Symposium on Embrittlement of Zircaloy by Oxidation," Sixth Water-Reactor-Safety Research Information Meeting, National Bureau of Standards, Gaithersburg, MD (Nov 6, 1978).

5. Light-water-reactor Safety Research Program: Quarterly Progress Report, January-March 1978, Sec. III, "Mechanical Properties of Zircaloy Containing Oxygen," ANL-78-49, NUREG/CR-0201, pp. 45-63 (July 1978).

6. Light-water-reactor Safety Research Program: Quarterly Progress Report, July-September 1978, Sec. III, "Mechanical Properties of Zircaloy Containing Oxygen," ANL 78-107, NUREG/CR-0547, pp. 27-46 (Jan 1979).

7. Light-water-reactor Safety Research Program: Quarterly Progress Report, July-September 1977, Sec. III, "Mechanical Properties of Zircaloy Containing Oxygen," ANL-78-3, pp. 47-75 (Jan 1978).

8. G. Östberg, Determination of Hydride Solubility in Alpha Phase Zirconium, Zircaloy-2, and Zircaloy-4, J. Nucl. Mater. $\underline{5}$, 208-15 (1962).

9. R. P. Elliott, Constitution of Binary Alloys, 1st Supplement, McGraw-Hill, New York, p. 513 (1965).

10. Light-water-reactor Safety Research Program: Quarterly Progress Report, April-June 1978, Sec. III, "Mechanical Properties of Zircaloy Containing Oxygen," ANL-78-77, NUREG/CR-0423, pp. 19-42 (Dec 1978).

11. H. M. Chung, A. M. Garde, and T. F. Kassner, "Development of an Oxygen Embrittlement Criterion for Zircaloy Cladding Applicable to LOCA Conditions in Light-water Reactors," Proc. ASTM 4th Int. Conf. on Zirconium in Nuclear Industry, Stratford-on-Avon, England (June 27-29, 1978).

12. D. O. Hobson, "Ductile-Brittle Behavior of Zircaloy Fuel Cladding," Proc. ANS Topical Meet. on Water-Reactor Safety, CONF. 730304, pp. 274-288 (1973).

13. Light-water-reactor Safety Research Program: Quarterly Progress Report, October-December 1977, Sec. III, "Mechanical Properties of Zircaloy Containing Oxygen," ANL-78-25. NUREG/CR-0089, pp. 31-44 (May 1978).

14. H. M. Chung and T. F. Kassner, Deformation Characteristics of Zircaloy Cladding in Vacuum and Steam Under Transient-heating Conditions: Summary Report, ANL-77-31, NUREG/CR-0344 (July 1978).

15. K. Homma, T. Furuta, and S. Kawasaki, Behavior of Zircaloy Cladding Tube in a Mixed Gas of Hydrogen and Steam, JAERI-7131, Japan Atomic Energy Research Institute (June 1977).

Distribution for NUREG/CR-0828 (ANL-79-18)

Internal:

R. V. Laney	P. A. Lottes	D. R. Pepalis
J. A. Kyger	R. P. Anderson	E. Stefanski
J. R. Honekamp	M. Ishii	W. D. Jackson
J. W. O'Kelley	R. P. Stein	Y. Y. Liu
J. W. Boudrot	R. E. Henry (2)	S. M. Gehl
M. V. Nevitt	L. McUmber	T. F. Kassner (2)
B. R. T. Frost	W. Wang	H. M. Chung
R. Avery	F. L. Yaggee	A. M. Garde
R. W. Weeks	Y. S. Cha	J. A. Buzzell
M. Blander	J. C. Leung	J. Rest (2)
C. E. Dickerman	L. A. Neimark	A. B. Krisciunas
L. W. Deitrich	R. B. Poeppel	ANL Contract File
E. E. Gruber	D. Stahl	ANL Libraries (2)
R. G. Palm		TIS Files (6)

External:

NRC, for distribution per R-2, R-3, R-4 (494)
DOE-TIC (2)
Manager, Chicago Operations and Regional Office, DOE
Chief, Office of Patent Counsel, DOE-CORO
President, Argonne Universities Association
Reactor Analysis and Safety Division Review Committee:
 S. Baron, Burns and Roe, Inc.
 J. R. Dietrich, Combustion Engineering, Inc.
 W. Kerr, U. Michigan
 M. Levenson, Electric Power Research Inst.
 S. Levy, S. Levy, Inc.
 D. Okrent, U. California, Los Angeles
 N. C. Rasmussen, Massachusetts Inst. Technology
Materials Science Division Review Committee:
 E. A. Aitken, General Electric Co., Sunnyvale
 G. S. Ansell, Rensselaer Polytechnic Inst.
 R. W. Balluffi, Massachusetts Inst. Technology
 R. J. Birgeneau, Massachusetts Inst. Technology
 S. L. Cooper, U. Wisconsin
 C. Laird, U. Pennsylvania
 M. T. Simnad, General Atomic
 C. T. Tomizuka, U. Arizona
 A. R. C. Westwood, Martin Marietta Labs.